A linear and regularized ODF estimation algorithm to recover multiple fibers in Q-Ball imaging

Maxime Descoteaux, Elaine Angelino, Shaun Fitzgibbons, Rachid Deriche

INSTITUT NATIONAL DE RECHERCHE EN INFORMATIQUE ET EN AUTOMATIQUE

A linear and regularized ODF estimation algorithm to recover multiple fibers in Q-Ball imaging

Maxime Descoteaux — Elaine Angelino — Shaun Fitzgibbons — Rachid Deriche

N° 5768

November 2005

Thème BIO

ISSN 0249-6399 ISRN INRIA/RR--5768--FR+ENG

A linear and regularized ODF estimation algorithm to recover multiple fibers in Q-Ball imaging

Maxime Descoteaux* , Elaine Angelino† , Shaun Fitzgibbons‡ , Rachid Deriche§

Thème BIO —Systèmes biologiques
Projet Odyssée

Rapport de recherche n° 5768 —November 2005 — 45 pages

Abstract: Due the well-known limitations of diffusion tensor imaging (DTI), high angular resolution diffusion imaging is currently of great interest to characterize voxels containing multiple fiber crossings. In particular, Q-ball imaging (QBI) is now a popular reconstruction method to obtain the orientation distribution function (ODF) of these multiple fiber distributions. The latter captures all important angular contrast by expressing the probability that a water molecule will diffuse into any given solid angle. However, QBI and other high order spin displacement estimation methods involve non-trivial numerical computations and lack a straightforward regularization process. In this paper, we propose a simple linear and regularized analytic solution for the Q-ball reconstruction of the ODF. First, the signal is modeled with a physically meaningful high order spherical harmonic series by incorporating the Laplace-Beltrami operator in the solution. This leads to an elegant mathematical simplification of the Funk-Radon transform using the Funk-Hecke formula. In doing so, we obtain a fast and robust model-free ODF approximation. We validate the accuracy of the ODF estimation quantitatively using the multi-tensor synthetic model where the exact ODF can be computed. We also demonstrate that the estimated ODF can recover known multiple fiber regions in a biological phantom and in the human brain. Another important contribution of the paper is the development of ODF sharpening methods. We show that sharpening the measured ODF enhances each underlying fiber compartment and considerably improves the extraction of fibers. The proposed techniques are simple linear transformations of the ODF and can easily be computed using our spherical harmonics machinery.

Key-words: Q-ball imaging, orientation distribution function (ODF), spherical harmonics, funk-radon transform, funk-hecke formula

* Maxime.Descoteaux@sophia.inria.fr
† angelino@fas.harvard.edu
‡ fi tzgibb@fas.harvard.edu
§ Rachid.Deriche@sophia.inria.fr

Estimation linéaire et régularisation de l'ODF pour la détection de croisements de fibres en imagerie par Q-ball

Résumé : Contrairement au tenseur de diffusion classique (DTI), l'IRM de diffusion à haute résolution angulaire permet de décrire les croisements de faisceaux de fibres au sein de la matière blanche. La reconstruction de la function de distribution d'orientations des fibres (ODF) par Q-ball est une technique largement répandue dans l'étude de ces croisements dans un cadre de segmentation ou de tractographie. L'ODF nous renseigne sur la distribution de probabilité des directions de diffusion des molécules d'eau présentes dans la matière blanche. Cependant, cette méthode ainsi que les autres techniques d'estimation à haute résolution angulaire sont basées sur des solutions numériques complexes et sans aucun processus de régularisation. Dans ce rapport, nous proposons une solution linéaire et régularisée pour l'estimation de l'ODF à partir de l'imagerie par Q-ball. Nous approximons d'abord le signal par une série d'harmoniques sphériques lissée grâce à l'opérateur Laplace-Beltrami. Cette formulation nous permet de dériver une simplification élégante de la transformée de Funk-Radon en utilisant le théorême de Funk-Hecke. Nous obtenons alors un algorithme robuste et rapide pour l'estimation de l'ODF. L'efficacité et la précision de l'approximation sont évaluées sur des données synthétiques et réelles. Nous faisons varier les paramètres importants dans la formation de l'image et observons les différentes répercussions sur la forme des ODFs. Enfin, nous démontrons que le "sharpening" des ODFs (rehaussement des maxima) améliore considérablement l'extraction des directions des multiples fibres sousjacentes.

Mots-clés : Imagerie par Q-ball, function de distribution d'orientations (ODF), harmoniques sphériques, transformée de funk-radon, formule de funk-hecke

Contents

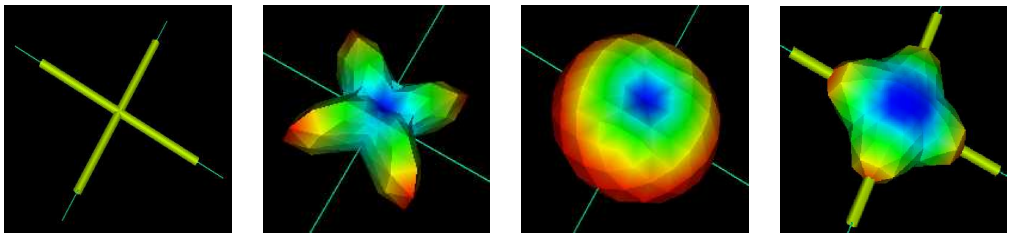

fiber distribution | true diffusion profile | DTI diffusion profile | ODF

Figure 1: Diffusion profile estimate from DTI fails to recover multiple fiber orientation. The maxima of the diffusion profile do not agree with thin green lines corresponding to the true synthetic fiber directions whereas maxima of the ODF do.

1 Introduction

Diffusion MRI is the only non-invasive tool to obtain information about the neural architecture in vivo and it is used to understand functional coupling between cortical regions of the brain, for characterization of neuro-degenerative diseases, for surgical planning and for other medical applications. The method is based on the Brownian motion of water molecules in normal tissues and the observation that molecules tend to diffuse along fibers when contained in fiber bundles [4, 15]. Using classical diffusion tensor imaging (DTI), several methods have been developed to segment and track white matter fibers in the human brain [7, 14, 16, 17, 36, 41, 43]. However, the theoretical basis for the DTI model assumes that the underlying diffusion process is Gaussian. While this approximation is adequate for voxels in which there is only a single fiber orientation (or none), it breaks down for voxels in which there is more complicated internal structure, as seen in Fig. 1 with an example of two fibers crossing. The model is not flexible enough to describe several major diffusion directions and therefore gives an over-smoothed estimation of the water molecule diffusion profile. This is an important limitation, since resolution of DTI acquisition is between 1mm^3 and 3mm^3 while the physical diameter of fibers can be less than 1μm and up to 30 μm [27]. From anisotropy measure maps, we know that many voxels in diffusion MRI volumes potentially have multiple fibers with crossing, kissing or diverging configurations.

To date, this is a reason why clinicians and neurosurgeons have been skeptical of tracking and segmentation methods developed on DTI data. They have doubts on the principal direction followed to track fiber bundles. In the presence of multiple fibers, the diffusion profile is oblate or planar and there is no unique principal direction (Fig. 1). This is why recent research has been done to generalize the existing diffusion model with new higher resolution acquisition techniques such as Q-Space Imaging (QSI) [42] and High Angular Resolution Diffusion Imaging (HARDI) [37]. There are currently two classes of high order processing methods for these high resolution acquisition techniques. The first is based on apparent diffusion coefficient (ADC) modeling [2, 9, 12, 21, 22] and the other is based on the estimation of the probability density function of the average spin displacement of water molecules [1, 5, 7, 8, 20, 25, 26, 35, 38, 39].

In the first case, the natural generalization of classical DTI is to describe the ADC profile with a higher order diffusion tensor (HODT) [21, 24, 25]. This formulation has been shown ([10, 21]) to be equivalent to spherical harmonic series approximation techniques [2, 10, 12], where non-Gaussian diffusion can be characterized using high order anisotropy measures based on the HODT description of the spherical harmonic series coefficients of the ADC profile [10]. However, as discussed in [19], one shortcoming of ADC-based models is that they are based on the assumption that the signal decays mono-exponentially which is not the case for all diffusion encoding directions when there is an underlying non-Gaussian diffusion. Another disadvantage of ADC modeling is that the ADC is measured in signal space, *q-space*, where the maxima of the ADC profile do not match the underlying fiber orientations (Fig. 1). Thus, to date, no robust and theoretically established algorithms have been developed to extract fiber directions from ADC-based approaches although the recent paper of Ozarslan et al. [22] shows how to transform the diffusion profile into a probability profile. From the latter profile, it is possible to extract the fiber orientations. We will discuss this paper in detail later in Section 7.

The general and proper setting for fiber analysis is real space. Hence, the focus of this paper is on the second class of algorithms, where functions of interest are defined in real space. In this case, techniques generally approximate the diffusion probability density function (PDF) or variants of it arising from various types of high angular resolution signal data. The important functions in the literature are the Persistent Angular Structure (PAS) [20] of the PDF, the fiber orientation distribution (FOD) [1, 35] and the diffusion orientation distribution function (ODF) [38]. We will review them in the next section and mainly focus on the ODF, which captures important angular information and can be viewed has the probability that the water molecule will diffuse in any solid angle. For all these high angular functions, the important property is that their maxima agree with the underlying fiber distribution (e.g. ODF in Fig. 1). However, these methods are all based on non-trivial numerical methods and lack a straightforward regularization process and fail to take into account the useful tools for both estimation and regularization that have been developed for the fitting of the ADC profile.

In this article, we propose a simple linear and regularized solution for the popular Q-ball imaging approximation of the ODF. It is obtained by modeling the signal with a high order spherical harmonic series using a Laplace-Beltrami regularization method developed for the ADC profile estimation in [10]. This spherical harmonics representation leads to an elegant mathematical simplification of the Funk-Radon transform of the measured signal using the Funk-Hecke formula. In doing so, we obtain a fast algorithm for the extraction of a robust model-independent ODF approximation at each voxel of the raw HARDI data. We evaluate the performance of our algorithm on synthetic data, where we study the effect of the b-value parameter and noise level in the input signal. We find that ODF sharpening, i.e. the enhancement of the peaks of the ODF, can improve the characterization of the underlying fiber distribution when fibers are close to one another and the estimation is too smooth. We propose a Laplacian-based approach and a new delta function transform method. Finally, we illustrate the potential of our fiber detection technique on real data where we recover multiple fiber crossings in a biological rat spinal chord phantom and on known regions of interest in the human brain.

2 High Angular Resolution Reconstruction Methods

In this section, we give a survey of the state of the art high resolution imaging techniques designed to better describe the complexity of water motion. In particular, we develop the theory of the Q-ball imaging sequence, which will be the main focus of the paper hereafter. We are interested in recovering the fiber distribution at every voxel of the data. As we will see, many functions are used in the literature to measure the diffusion properties of the underlying fiber bundles, such as the diffusion probability density function (PDF), the persistent angular structure (PAS), the fiber orientation distribution (FOD) and the diffusion orientation distribution function (ODF).

2.1 Q-Space Imaging

Stejskal and Tanner [34] showed that if the gradient pulse duration δ is short enough for the diffusion of the water molecule to be negligible during that time, then the signal attenuation $S(\mathbf{q})$ is expressed as the 3-dimensional (3D) Fourier transform $\mathcal{F}$ of the ensemble average propagator P,

$$\frac{S(\mathbf{q})}{S_0} = \int P(\mathbf{r}) e^{-2\pi i \mathbf{q}^T \mathbf{r}} d\mathbf{r} = \mathcal{F}[P(\mathbf{r})], \tag{1}$$

where the value of $\mathbf{q}$ is given by $\mathbf{q} = \gamma \delta \mathbf{G}/2\pi$, with γ the nuclear gyromagnetic ratio for water protons and $\mathbf{G}$ the applied diffusion gradient vector, and S_0 is the baseline image acquired without any diffusion gradients. $P(\mathbf{r})$ is the probability averaged over a voxel that a spin starting at a given point in the voxel will have displaced by some radial vector $\mathbf{r}$ in time τ. It is this probability density function (PDF) that we optimally want to obtain from the raw signal measurements. In classical DTI, the problem is simplified by assuming that this PDF can be described by a zero-mean Gaussian distribution which has its well-known limitations in the presence of multiple fibers.

Eq. 1 suggests the fairly straightforward means of extracting the PDF from measurements in q-space by measuring the signal on a Cartesian grid of points in q-space and then taking the 3D inverse Fourier transform to obtain an approximated PDF. This technique is called q-space imaging (QSI) or diffusion spectrum imaging (DSI) [42] and it has been used with some success. It has also been used with a high order tensor modeling of the diffusion profile in [21]. However, it is restricted by severe limitations. Firstly, in order to resolve features in the PDF on the order of some scale 1/a, it requires a box of side length $>$ a in q-space. In practice, this requires many measurements and very large q-values compared to those used on conventional scanners. As we want δ small to verify the narrow pulse approximation, the gradients $\mathbf{G}$ must be very high which creates eddy current distortions. This results not only in an engineering limitation as to the maximal q-values attainable, but also in a signal to noise ratio (SNR) problem. The latter arises from the fact that the measured quantity is signal attenuation, which is given by

$$S(\mathbf{q}) = S_0 e^{-\tau \mathbf{q}^T D \mathbf{q}}, \tag{2}$$

where $D(\mathbf{q}) = \mathbf{q}^T D \mathbf{q}$ is the apparent diffusion profile. Thus, for large $\mathbf{q}$, the true signal quickly falls off, while the background noise is relatively unaffected, thus resulting in very noisy data measurements for some regions of the grid. It is worth mentioning that the signal attenuation is also

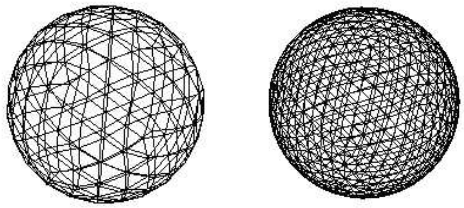

162 points 642 points

Figure 2: Discrete samplings of the sphere for different numbers of gradient directions corresponding to order 3 and order 4 tessellations of the sphere respectively.

often written with respect to unit vector, $\mathbf{u} = \mathbf{q}/|\mathbf{q}|$, and the introduced b-factor, $b = \tau|\mathbf{q}|^2$. We thus obtain a signal attenuation given by

$$S(\mathbf{u}) = S_0 e^{-\tau|\mathbf{q}|^2 \mathbf{u}^T D \mathbf{u}} = S_0 e^{-b\mathbf{u}^T D \mathbf{u}}. \tag{3}$$

Hence, the grid spacing needs to be on the order of $1/b$ in order to obtain a box in real space on the order of side length b. This results in a major practical problem because of the number of samples required to tightly fill in a large 3D Cartesian grid. This problem is mainly one of imaging time, which increases like N^3 as the size of the grid is increased, and makes it impracticable to obtain very high resolution images using the q-space method. Note that for visualization, the estimated diffusion PDF is usually projected onto the sphere to obtain the diffusion ODF which is more illustrative.

2.2 High Angular Resolution Diffusion Imaging

As a result of the DSI limitations, other techniques have been developed to attempt to extract the desired information in a more efficient way. One such clinically feasible approach is high angular resolution diffusion imaging (HARDI) [39]. The idea is to sample a single sphere with N discrete gradient directions, as in Fig. 2, and measure the signal attenuation along each direction. In practice, one can sample only the hemisphere as the diffusion PDF is assumed to be symmetric. Given these discrete measurements over the surface of the sphere, several methods have been proposed to extract the diffusion PDF.

2.2.1 Multi-fiber Gaussian Models

Tuch et al. [39] proposed to model the HARDI signal as a finite mixture of n Gaussians to obtain the diffusion PDF as

$$P(\mathbf{r}) = \sum_{i=1}^{n} \left(\frac{1}{(4\pi\tau)^3 |\mathbf{D}_i|} \right)^{1/2} \exp\left(\frac{-\mathbf{r}^T \mathbf{D}_i^{-1} \mathbf{r}}{4\tau} \right). \tag{4}$$

However, this Gaussian mixture modeling requires an iterative gradient descent for the reconstruction of the PDF which is unstable and sensitive to the starting point selected. It also depends on a possibly over-simplified and incorrect fiber model when fixing the number of fiber compartments.

2.2.2 Persistent Angular Structure MRI

Jansons and Alexander [20] proposed the radially persistent angular structure (PAS) $\hat{p}$ of the diffusion PDF by assuming independence of the angular and radial structure,

$$P(\mathbf{r}) = \frac{1}{r_0^2}\hat{p}(\hat{r})\delta(|\mathbf{r}| - r_0). \tag{5}$$

Intuitively, this forces probabilities to be non-zero only on a spherical shell of radius r_0. Plugging Eq. 5 in Eq. 1 and using some maximum entropy cost function, they solve for the PAS function $\hat{p}(\hat{r})$ by fitting the raw data with a nonlinear iterative algorithm. The PAS is the function on the sphere that best describes the signal measurements and intuitively represents the relative mobility of spins in each direction. Although is it not obvious why the peaks of the PAS should agree with the underlying fiber distribution, the method seems accurate [1].

2.2.3 Spherical Deconvolution

A different approach proposed by Tournier et al. [35] is to view the HARDI signal on the surface of the sphere as the convolution over the sphere of the response function of a single fiber with the fiber orientation distribution (FOD). As we will see in the next section, the FOD is a different function than the diffusion ODF even though both functions can have multiple peaks each representing an underlying fiber compartment. In [35], a linear basis of spherical harmonics and rotational harmonics is used to parametrize the signal and fiber response function respectively. The FOD is then obtained by simple matrix multiplication. This method shows nice results recovering fibers crossing but has some reported instabilities ([1, 35]) for high harmonic orders. Alexander recently showed in [1] that an improved FOD could be extracted using a non-linear maximum entropy implementation of the spherical deconvolution, inspired by the earlier PAS solution in [20]. In both deconvolution methods, the disadvantage is that a fiber response function needs to be assumed a priori to use as deconvolution kernel. In [1], the response function is a standard Gaussian kernel whereas in [35], the response function is estimated from the signal attenuation profile in 300 voxels with highest fractional anisotropy, regions likely to have a single coherent fiber population. We now introduce Q-ball imaging which has the advantage of being model-independent.

2.2.4 Q-Ball Imaging

Tuch [37, 38] showed that the diffusion orientation distribution function (ODF) could be estimated directly from the raw HARDI measurements on a single sphere of q-space without computing the full diffusion PDF before projecting onto the sphere. The basic assumption of QBI is that angular information is enough to recover fiber orientation distributions (forgetting about radial information). As such, QBI is a modality which takes advantage of the fact that significantly less information is

required to construct an angular function in real space than is required to construct a volume function as DSI does. Specifically, QBI seeks to reconstruct the diffusion ODF, a function defined as the radial projection of the diffusion PDF as

$$\Psi(\mathbf{u}) = \int_0^\infty P(\alpha \cdot \mathbf{u}) d\alpha, \tag{6}$$

where $\mathbf{u}$ is restricted to be a unit vector. Thus, the ODF is a function on the unit sphere describing the probability averaged over the voxel that a particle will diffuse into any given solid angle.

To calculate the ODF, the QBI modality uses the Funk-Radon transform (FRT) $\mathcal{G}$, a transformation from the unit sphere to itself [38]. In order to find the Funk-Radon transformed value of the signal on the sphere at a given point $\mathbf{u}$, one needs to first find the plane through the origin with normal vector $\mathbf{u}$ and then compute the one dimensional integral over the intersection of that plane with the function on the original sphere. Intuitively, to find the new value at an arbitrarily defined "pole", one integrates over the corresponding "equator" or great circle. This can be written explicitly as

$$\mathcal{G}[f(\mathbf{w})](\mathbf{u}) = \int \delta(\mathbf{u}^T \mathbf{w}) f(\mathbf{w}) d\mathbf{w} \tag{7}$$

where **u** and **w** are constrained to be unit vectors. To see why this spherical transformation is close to the ODF, Tuch [38, Appendix A] proves that the mathematical relation between the ODF and the FRT is given by

$$\Psi(\mathbf{u}) \approx \mathcal{G}_{q'}[S(\mathbf{q})](\mathbf{u}) = 2\pi q' \int P(r, \theta, z) J_0(2\pi q' r) r dr d\theta dz. \tag{8}$$

In Appendix A, we reproduce a more detailed proof and introduce the important Fourier analysis tools that clarify the relation between the FRT and the ODF. From this proof and comparing Eqs. 6 and 8, it clear that the FRT is a smoothed version of the true ODF. In fact, the higher q', which is directly proportional to the b-value, the closer the FRT approximation is to the exact ODF as the zeroth-order Bessel function J_0 gets sharper and approaches a Dirac delta function. Fortunately, the values of b required to satisfy this condition are relatively small ($b = 4000$s/mm^2 used in [37]) compared to the maximal values of b required for the use the DSI technique ($b = 20000$s/mm^2 used in [42] and $b = 60000$s/mm^2 used in [21]).

In practice, the Funk-Radon transform can be implemented by a matrix multiplication. However, computing this matrix involves several non-trivial numerical computations. In particular, a regridding and an interpolation of the spherical input data is needed to compute the equator points in the FRT integral of Eq. 7 since many points outside the actual measurements are required. The algorithm is clearly sketched in [38, Tbl. 1]. Note that this interpolation requires a good a priori basis function and many sampling directions are required to obtain a good QBI reconstruction. In fact, Tuch's implementation [38] uses a fivefold tessellated icosahedron (252 samples) and a regridding of the signal onto equators around vertices of a fivefold tessellated dodecahedron (48 x 755 = 36240 points). Hence, it is a method that is still computationally intensive to implement in practice. In current research, most often a standard HARDI acquisition is used with relatively low b-values, from which the diffusion ODF is computed with the Funk-Radon transform.

Regardless, the QBI reconstruction has several advantages that have made it a popular high angular resolution reconstruction in many recent works [7, 18, 26, 29] for regularization and for fiber tracking. The ODF description is intuitive and gives a good representation of the underlying fiber distribution. Moreover, in theory, samples are only taken on a single sphere in q-space and thus, the imaging time is much smaller than that of the DSI despite significantly higher angular resolution measurements. Furthermore, since a relatively small constant value of q' can be chosen, the signal to noise ratio (SNR) is greatly improved.

We now apply our recent technique for the approximation of functions on the sphere from noisy sparse data in order to obtain a robust signal estimation with a regularization procedure. This method was developed in [10] to model the apparent diffusion profile using spherical harmonics. It was shown to be very useful to characterize isotropic, 1- and multi-fiber fiber distributions. We will demonstrate that the use of a modified spherical harmonics basis can describe the input signal and greatly simplify the Funk-Radon transform integral.

3 Analytic ODF estimation with the Funk-Radon Transform

Before describing our new Funk-Radon derivation based on a spherical harmonics formulation, we review the important points of our previous approach [10] in which we have developed a simple and efficient way to estimate the continuous function on a Q-ball from a discrete sampling of measurements. We proposed a real and symmetric modified spherical harmonics basis capturing the physical constraints of the diffusion MRI acquisition and obtained a simple closed form matrix multiplication algorithm. Using the smoothing application of the Laplace-Beltrami operator for functions on the sphere, we showed it is possible to incorporate a regularization term in the estimation. We review the key parts here and refer the reader to [10] for extensive details and examples.

3.1 Signal Approximation with the Spherical Harmonics

The spherical harmonics (SH), normally indicated by Y_ℓ^m (ℓ denotes the order and m the phase factor), are a basis for complex functions on the unit sphere. Explicitly, they are given as follows

$$Y_\ell^m(\theta,\phi) = \sqrt{\frac{2\ell+1}{4\pi}\frac{(\ell-m)!}{(\ell+m)!}} P_\ell^m(\cos\theta) e^{im\phi} \tag{9}$$

where (θ,ϕ) obey physics convention ($\theta \in [0,\pi], \phi \in [0,2\pi)$) and P_ℓ^m is an associated Legendre polynomial. For $\ell = 0, 2, 4, \ldots, \ell_{max}$ and $m = -\ell, \ldots, 0, \ldots, \ell$, we let
$j = j(\ell,m) = (\ell^2+\ell+2)/2 + m$ and define our modified basis as

$$Y_j = \begin{cases} \frac{\sqrt{2}}{2}((-1)^m Y_\ell^m + Y_\ell^{-m}), & \text{if } -\ell \le m < 0 \\ Y_l^0, & \text{if } m = 0 \\ \frac{\sqrt{2}i}{2}((-1)^{m+1} Y_\ell^m + Y_\ell^{-m}), & \text{if } 0 < m \le \ell \end{cases} \tag{10}$$

It is designed to be symmetric, as only even order SH are considered and it is shown in [10] to be real. The angular frequency of the approximation increases with $\ell_{\max}$ and the ratios in front of each

term also ensure that the modified basis is orthonormal with respect to the inner product $< f, g >= \int_\Omega \bar{f} g d\Omega$, where Ω denotes integration over the unit sphere and $\bar{f}$ is the complex conjugate of f. We thus approximate the signal at each of the n_s gradient direction i as

$$S(\theta_i, \phi_i) = \sum_{j=1}^{N} c_j Y_j(\theta_i, \phi_i) \tag{11}$$

where $N = (\ell+1)(\ell+2)/2$ is the number of terms in the SH series of order ℓ. We can write the set of equations as an over-determined linear system $S = BC+$error, where B is the matrix constructed with the modified spherical harmonics basis

$$B = \begin{bmatrix} Y_1(\theta_1, \phi_1) & Y_2(\theta_1, \phi_1) & \cdots & Y_N(\theta_1, \phi_1) \\ \vdots & \vdots & \ddots & \vdots \\ Y_1(\theta_{n_s}, \phi_{n_s}) & Y_2(\theta_{n_s}, \phi_{n_s}) & \cdots & Y_N(\theta_{n_s}, \phi_{n_s}) \end{bmatrix}$$

and C is the vector of SH coefficients c_j. We want to solve for the SH series coefficients c_j, where $c_j = \int_\Omega S(\theta_i, \phi_i) Y_j(\theta_i, \phi_i) d\Omega$. At this point, instead of evaluating the integrals directly [12] or performing a simple least-squared minimization as in [2, 35], we add local regularization to our fitting procedure. We define a measure of the deviation from smoothness E of a function f defined on the unit sphere as $E(f) = \int_\Omega (\triangle_b f)^2$, where $\triangle_b$ is the Laplace-Beltrami operator. The Laplace-Beltrami operator, which is the Laplacian operator in spherical coordinates, is a natural measure of smoothness for functions defined on the unit sphere. It has a very simple expression as it must satisfy the relation $\triangle_b Y_\ell^m = -\ell(\ell+1) Y_\ell^m$. Note that this relation also holds for our modified SH basis. As a result, using the orthornormality of the modified SH basis, the above functional E can be rewritten straightforwardly as

$$E(f) \quad = \quad \int_\Omega \triangle_b \left(\sum_p c_p Y_p \right) \triangle_b \left(\sum_q c_q Y_q \right) d\Omega = \sum_{j=1}^{N} c_j^2 \ell_j^2 (\ell_j + 1)^2 = C^T \mathbf{L} C, \tag{12}$$

where L is simply the N x N matrix with entries $\ell_j^2(\ell_j+1)^2$ along the diagonal. Therefore, the quantity we wish to minimize can be expressed in matrix form as

$$M(C) = (BC - S)^T (BC - S) + \lambda C^T L C,$$

where λ is the weight on the regularization term. The coefficient vector minimizing this expression can then be determined just as in the standard least-squares fit ($\lambda = 0$), from which we obtain the generalized expression for the desired spherical harmonic series coefficient vector

$$\boxed{C = (B^T B + \lambda L)^{-1} B^T S.} \tag{13}$$

From this SH coefficient vector we can recover the signal on the Q-ball for any (θ, ϕ) as

$$S(\theta, \phi) = \sum_{j=1}^{N} c_j Y_j(\theta, \phi). \tag{14}$$

Intuitively, this approach penalizes an approximation function for having higher order terms in its modified SH series. Therefore, higher order terms will only be included in the fit if they significantly improve the overall accuracy of the approximation. This eliminates most of the high order terms due to noise while leaving those that are necessary to describe the underlying function. However, obtaining this balance depends on choosing a good value for the parameter λ. We use the *L-curve* numerical method [13] and experimental simulations to determine the best smoothing parameter [10].

3.2 Funk-Radon Transform Using Spherical Harmonics

Not only do spherical harmonics allow the definition a simple regularization procedure but we now show that they also simplify greatly the computation of the Funk-Radon transform using the Funk-Hecke formula. Here, we write the dot product between two vectors $\mathbf{x}, \mathbf{u} \in \mathbb{R}^3$ as $\mathbf{x}^T\mathbf{u}$. The key observation is that any continuous function f on the interval $[-1, 1]$ extends to a continuous function of two variables $g(\mathbf{x}, \mathbf{u})$ on the sphere defined by $g(\mathbf{x}, \mathbf{u}) = f(\mathbf{x}^T\mathbf{u})$. With this formulation, the Funk-Hecke formula is a theorem that relates the inner product of any spherical harmonic with the projection on the sphere of any continuous function $f(t)$ defined on the interval $[-1, 1]$. The theorem was first published by Funk [1916] and a little later by Hecke [1918] [3, chap.9].

> **Funk-Hecke Theorem:** Let f(t) be continuous on $[-1, 1]$ and H_ℓ any spherical harmonic of order ℓ. Then, given a unit vector $\mathbf{x}$
>
> $$\int_{|\mathbf{u}|=1} f(\mathbf{x}^T\mathbf{u}) H_\ell(\mathbf{u}) d\mathbf{u} = \lambda(\ell) S_\ell(\mathbf{x}), \tag{15}$$
>
> where
>
> $$\lambda(\ell) = \frac{2\pi}{P_\ell(1)} \int_{-1}^{1} P_\ell(t) f(t) dt$$
>
> with P_ℓ the Legendre polynomial of degree ℓ.

In particular, this formula gives a powerful tool for evaluating integrals over the sphere where the integrand is a product of a spherical harmonic and a function continuous on $[-1, 1]$.

In our case, recall that the Funk-Radon transform of the signal in a unit direction $\mathbf{x}$ is the integral over the great circle perpendicular to $\mathbf{x}$. Hence, we have

$$\begin{aligned} \mathcal{G}[S](\mathbf{x}) &= \int_{|\mathbf{u}|=1} \delta(\mathbf{x}^T\mathbf{u}) S(\mathbf{u}) d\mathbf{u} \\ &= \int_{|\mathbf{u}|=1} \delta(\mathbf{x}^T\mathbf{u}) \sum_j c_j Y_j(\mathbf{u}) d\mathbf{u} \\ &= \sum_j c_j \underbrace{\int_{|\mathbf{u}|=1} \delta(\mathbf{x}^T\mathbf{u}) Y_j(\mathbf{u}) d\mathbf{u}}_{I} \end{aligned} \tag{16}$$

Note that if the Dirac delta function δ were continuous on the interval $[-1, 1]$, I could be directly evaluated using the Funk-Hecke formula of Eq. 15. However, $\delta(t)$ is discontinuous at zero. Hence,

we approximate the Dirac delta function with a Gaussian of decreasing variance given by

$$\delta_n(x) = \frac{n}{\sqrt{\pi}} e^{-n^2 x^2}.$$

In Appendix B, we show that the latter is a delta sequence. That is, letting the variance of the Gaussian tend to zero, we show that the sequence of decreasing Gaussians converges to a Dirac delta function ($\lim_{n\to\infty} \delta_n = \delta$), i.e.

$$\lim_{n\to\infty} \int_{-\infty}^{\infty} \delta_n(x) f(x) \quad = \quad f(0). \tag{17}$$

Since the Gaussian is continuous on the interval $[-1, 1]$, the delta sequence δ_n is also continuous on $[-1, 1]$ for all n. Hence, we can evaluate I using the Funk-Hecke formula of Eq. 15 and the delta sequence property of Eq. 17. We obtain

$$\begin{aligned}
I(\mathbf{x}) &= \int \delta(\mathbf{x}^T\mathbf{u}) Y_j(\mathbf{u}) d\mathbf{u} \\
&= \int \lim_{n\to\infty} \delta_n(\mathbf{x}^T\mathbf{u}) Y_j(\mathbf{u}) d\mathbf{u} \\
&= \lim_{n\to\infty} \int \delta_n(\mathbf{x}^T\mathbf{u}) Y_j(\mathbf{u}) d\mathbf{u} \\
&= \tfrac{2\pi}{P_\ell(1)} \left(\lim_{n\to\infty} \int_{-1}^{1} \delta_n(t) P_\ell(t) dt \right) Y_j(\mathbf{x}) \qquad \text{(used Eq. 15)} \\
&= 2\pi \tfrac{P_{\ell(j)}(0)}{P_{\ell(j)}(1)} Y_j(\mathbf{x}) \qquad \text{(used Eq. 17)}
\end{aligned}$$

The beauty of the approach is that we have greatly simplified the Funk-Radon integral by finding an analytic solution. We thus avoid using numerical schemes to perform the FRT.

Therefore, referring back to Eq. 16, the Funk-Radon transform of a function given in terms of our modified spherical harmonic series in a given unit vector direction $\mathbf{x}$ is simply given by

$$\mathcal{G}[S(\mathbf{q})](\mathbf{x}) = \sum_j 2\pi \frac{P_{\ell(j)}(0)}{P_{\ell(j)}(1)} c_j Y_j(\mathbf{x}) \tag{18}$$

Thus, the spherical harmonics are eigenfunctions of the Funk-Radon transform with eigenvalues depending only on the order ℓ of the SH series. When the signal $S(\mathbf{q})$ is parametrized by the vector C of SH coefficients, i.e. $S = BC$, the analytic Funk-Radon transform which approximates the ODF is simply a diagonal linear transformation given by

$$\boxed{ODF \approx \mathcal{G}[S] = \begin{pmatrix} \ddots & & \\ & 2\pi \frac{P_{\ell(j)}(0)}{P_{\ell(j)}(1)} & \\ & & \ddots \end{pmatrix} \begin{pmatrix} \vdots \\ c_j \\ \vdots \end{pmatrix} = PC = P(B^TB - \lambda L)^{-1} B^T S.} \tag{19}$$

Hence, using the spherical harmonics for the approximation of the signal attenuation function at a given radius in q-space, the Q-ball imaging procedure is optimized in terms of accuracy and computational efficiency. The accuracy of the modified SH series approximation and the proposed Laplace-Beltrami regularization for spherical functions was established in [10] and the method is fast because the matrix of discrete spherical harmonics B and matrices P and L need only be computed once for the whole volume. This FRT is simpler to compute than the great circle integral proposed by Tuch [38].

4 Evaluating the ODF estimation

As discussed in [10], there are different existing synthetic fiber models, such as the hindered cylindrical model [32] and the multi-tensor model [2]. In this paper, we use the multi-tensor Gaussian fiber model as it is simple and leads to an analytic computation of the ODF. We generate synthetic HARDI data with 81 discrete directions on the hemisphere (Fig. 2 left) assuming human brain white matter profiles D_k with eigenvalues $[1700, 200, 200] \cdot 10^{-6}\text{mm}^2/\text{s}$. This model assumes that each fiber has a Gaussian distribution that describes it and that fibers do not exchange water molecules. Hence, we can generate the signal for n fibers using any rotation of the diffusion tensor D_k as

$$S(\mathbf{u}) = \sum_{k=1}^{n} p_k e^{-b\mathbf{u}^T D_k \mathbf{u}} \tag{20}$$

where p_k is the proportion of the k-th fiber in the voxel. We randomly select the p_k for each fiber as well as its orientation, subject to a minimum angle constraint. We add Rician noise [30, 31] in order to have S_0 signal with SNR ratio of $\sigma = S_0/\zeta$. SNR with $\zeta = 35$ is a typical value for current medical scanners [2, 37].

Computing the exact ODF using the multi-tensor is possible. The inverse Fourier transform of a Gaussian is another Gaussian which means that the diffusion PDF of the multi-tensor signal given in Eq. 20 is proportional to another sum of Gaussians. The exact ODF is given in Tuch [38, Eq.2] for a single Gaussian fiber with respect to diffusion time τ. We reproduce the exact ODF derivation in terms of the b-factor in Appendix C. Therefore, this gives an exact point-wise basis for comparison of ODFs generated from the multi-tensor Gaussian fiber model.

Hence, we generate 1000 random 1, 2, and 3 fiber distributions using the multi-tensor model described above for different b-values and noise levels, each time calculating the optimal regularization λ parameter (see [10]). We vary the noise level $\zeta = 5, 10, 20, 35$ to have a variation of poor, average and high quality signals. We use an order-8 SH approximation of the signal to obtain the coefficients C given by Eq. 13 and then apply the linear transformation P given in Eq. 19 to obtain the estimated ODF, f'.

Letting f represent the exact ODF for the fiber distribution, we can compute a simple Euclidean average of the squared error between f and f' over all n_s sampled points on the sphere as

$$[f, f'] = \frac{1}{n_s} \sum_{i=1}^{n_s} (f'_i - f_i)^2. \tag{21}$$

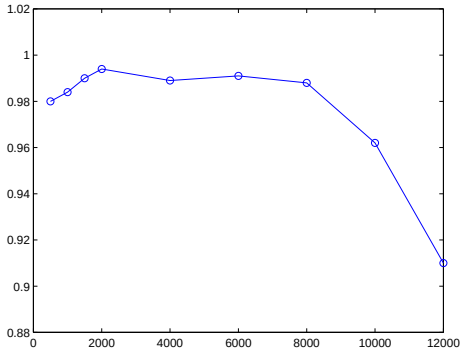

accuracy $< f, g >$ vs. b-value

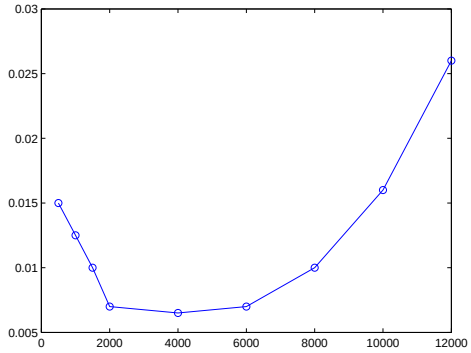

error $[f, g]$ vs. b-value

Figure 3: Plot of angular similarity measured with the inner product $< f, g >$ and with the pointwise Euclidean average $[f, g]$ versus b-value for optimal λ-regularization. Highest accuracy and lowest error are respectively observed for a plateau of high b-values between 2000 and 6000.

Moreover, we can compute another interesting comparison measure if we also describe f with an order-8 SH series. Although this last step is not exact, it leads to a very simple expression of the inner product between the two functions on the sphere. Recalling that our modified SH basis is real-valued and orthonormal, the inner product is

$$< f, f' >= \int_{\Omega} f \cdot f' d\Omega = \sum_{j} c_j \cdot d_j, \tag{22}$$

which is $C^T D$ in matrix form when C and D are the respective vectors of SH coefficients of f and f'. If we normalize such that $< f, f >=< f', f' >= 1$, this angularity measures is 1 when the functions are the same and its range is $[-1, 1]$.

As seen in Fig. 3, the estimation is very precise and we observe the same behavior using both angularity measure for comparison. For optimal b-value, the angularity measure using the inner product is > 0.99 and using the Euclidean averaged normalized error is < 0.01. As expected, we note that for low b-values, the Bessel function averaging effect mentioned earlier reduces the accuracy of the estimation. The high accuracy and low error are observed in a plateau of relatively high b-values between 2000 and 6000. Finally, observe that the best results are not necessarily for very high b-values because in this case, the signal is sharper and there is a large decrease in SNR. If the constant noise level were shifted, the location of the plateaus might shift as well. These results show that our ODF estimation is accurate and behaves as expected from reported results in the literature [35, 37] when assuming a multi-tensor model.

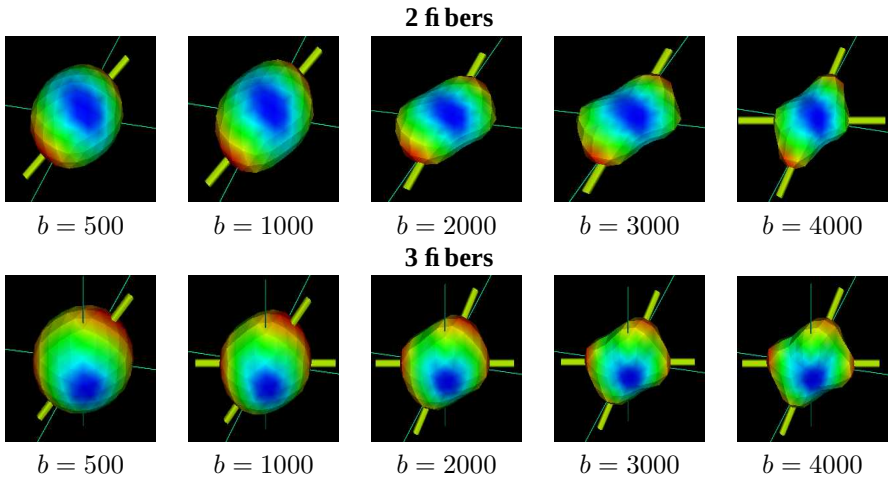

Figure 4: Synthetic ODFs for different b-values with detected fiber orientation.

5 Direct Fiber Extraction

It is generally assumed that the fiber directions are simply given by the local maxima of the ODF, where the function surpasses a certain threshold. This can be useful to extract local fiber orientation estimates for comparison with an estimated ground truth ([29]) and is also used for visualization purposes, overlaying the maxima over the PDF or ODF (e.g. [18, 35]). Most existing HARDI-based tractography algorithms (e.g [5, 7, 26]) use the full diffusion ODF or PDF to drive a front propagation or to generate most probable paths with Monte-Carlo simulations. However, in this paper, before tracking fiber bundles, we want to carefully evaluate the shape of the estimated ODF and how it changes under different parameter variations. We investigate how the b-value, the signal to noise ratio (SNR) and the truncation order-ℓ of the spherical harmonic (SH) series affect the ODF detection of the underlying fiber orientations. On top of the intrinsic zeroth-order Bessel function smoothing, it was also shown in [11] that the separability of the diffusion compartments depends on the magnitude of the b-value since the diffusion signal depends on the variance of each fiber distribution. Hence, at low b-values, there is overlap in the fiber compartments and the maxima are missed in the extraction procedure. This is seen in Fig. 4 where we have a 2- and a 3-fiber example with the detected fiber orientations. In the 2-fiber case, both fibers are identified only at high b-value of 4000 whereas in the 3-fiber case, the third fiber is never detected.

While it is common to use *min-max normalization* ([38]) and *minimum inscribed sphere* (MIS) subtraction ([25]) to enhance visual angular contrast when visualizing ODFs, these methods do not enhance the different underlying fiber compartments and do not improve maxima extraction. One way to deal with this problem is to introduce ODF sharpening methods to enhance each underlying fiber distribution. In many examples, the ODF approximation is too smooth without sharpening and

the maxima are difficult and sometimes impossible to differentiate. In fact, assuming the multi-tensor synthetic model and a white-matter human brain Gaussian fiber with eigenvalues $[1700, 200, 200]$ x 10^{-6} mm^2/s, one can show that if the signal is formed using the linear combination of two such fibers of equal magnitude and certain b-value, a simple maxima finding algorithm will fail to distinguish the two fibers if the angle between their respective directions is less than a certain angle θ (e.g. $\theta = 29^\circ$ when b = 1000). Appendix C shows the relation between this angle and the b-factor. With noise and random magnitude, the ability to distinguish fibers is even more compromised. Therefore, the need of a transformation that takes an ODF and produces a sharpened version is needed. This could potentially improve ODF-based tractography and segmentation results. We propose two methods for ODF sharpening. The first is based on the standard Laplacian sharpening used in image processing and the second is a transformation method using spherical harmonics and the Funk-Hecke formula as before. Both methods have very similar success for fiber detection.

5.1 Laplacian Sharpening

A simple idea is sharpening with the image Laplacian, a common tool in image processing. Given an image I, subtracting the Laplacian of the image times a weight factor gives a sharpened image, i.e. $I_{\text{sharp}} = I - \alpha\triangle I$. The weight determines the extent of the sharpening operation. We can express the same formula for a function f defined on the sphere $f_{\text{sharp}} = f - \alpha\triangle_b f$, where the Laplacian has been replaced by the Laplace-Beltrami operator for functions defined on the unit sphere. Recall that $\Delta Y_j = -\ell(\ell+1)Y_j$ and hence, if the estimated ODF is expressed in a SH series, $f = \sum_j c_j Y_j$ which is $F = BC$ in matrix form, we can express the sharpening as a linear transformation directly applied on the vector of SH coefficients C as

$$C_{\text{sharp}} \quad = \quad \begin{pmatrix} \vdots & & \\ & 1 + \alpha\ell(\ell+1) & \\ & \vdots & \end{pmatrix} C.$$

Thus, the Laplacian sharpening is a simple matrix multiplication producing $F_{\text{sharp}} = BC_{\text{sharp}}$.

5.2 Delta Function Transform (DFT) Sharpening

We also implement a sharpening method using the Funk-Hecke machinery developed earlier. The idea is inspired by Tournier et al. [35] spherical deconvolution where a particular fiber response function $R(\theta)$ must be assumed in order to deconvolve the measured signal to obtain the fiber orientation distribution. In our case, we also need to assume a-priori fiber response function $R(\theta)$ but define a different transform, the delta function transform (DFT). The latter relates the ODF and the function describing the fiber directions with delta functions, which is the sharper possible fiber distribution function.

Letting the k-th fiber direction be $\epsilon_{\mathbf{k}}$ and the evaluation point on the sphere defined by the unit vector $\mathbf{u}$, we define S_δ, the function describing each fiber direction as a Dirac delta function, i.e.

$$S_\delta(\mathbf{u}) = p_1\delta(\mathbf{u} - \epsilon_{\mathbf{1}}) + p_2\delta(\mathbf{u} - \epsilon_{\mathbf{2}}) + ...$$

Now, since the ODF $\Psi(\mathbf{u})$ for a single fiber is just a function of the angle between the point of evaluation and the fiber's primary axis, using linearity, we also have

$$\Psi(\mathbf{u}) = p_1 R(\mathbf{u} \cdot \epsilon_\mathbf{1}) + p_2 R(\mathbf{u} \cdot \epsilon_\mathbf{2}) + ...$$

where the p_k are the relative weights of each fiber and $R(t)$ is the under-determined 1D Gaussian profile derived in Appendix D describing the response of a single fiber in terms of the cosine of the angle between the point of evaluation and fiber's primary axis. From the definition of the delta function, it is immediate that the previous two equations can be merged into the delta function transform (DFT)

$$\Psi(\mathbf{u}) = \int_\Omega R(\mathbf{u} \cdot \epsilon) S_\delta(\epsilon) d\epsilon.$$

If we parametrize S_δ with a truncated spherical harmonic series such that $S_\delta(\mathbf{u}) = \sum_j^\infty k_j Y_j(\mathbf{u})$ and observe that $R(t)$ is continuous on $[-1, 1]$, we can use the Funk-Hecke formula to obtain the relation

$$\Psi(\mathbf{u}) = \sum_j^\infty k_j \lambda(\ell_j) Y_j(\mathbf{u}) \qquad \text{with} \qquad \lambda(\ell_j) = \frac{2\pi}{P_{\ell_j}(1)} \int_{-1}^{1} P_{\ell_j}(t) R(t) dt.$$

In this case, we can evaluate the integral numerically or precompute the exact definite integrals with Maple and tabulate them for order $\ell = 4, 6, 8, ...$ Hence, in matrix form, letting F represent the ODF, we have the DFT given by

$$F = \Lambda_R \cdot S_\delta$$

In theory, this transformation is invertible and thus, we could easily take a measured ODF to the desired delta function coefficients on the sphere, if infinite series were used. However, in practice, we deal with truncated spherical series of order $4, 6$ or 8 which are not enough to properly model delta functions. This is seen in Fig. 6, where the intermediate truncated spherical function, $S_\delta = \Lambda_R^{-1} \cdot F$, does not correspond to the expected sharp delta fiber response function but resembles a sharp version of the input signal S on the sphere (column 1 versus column 3 in Fig. 6).

To understand why this is so, we reproduced Tournier et al. [35, Fig.1] in Fig. 5 to illustrate what happens if we view the signal as the convolution of the response function R and the fiber distribution

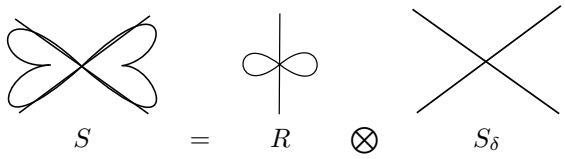

Figure 5: Tournier et al. [35] deconvolution assumption. The measured signal S is the convolution of the fiber response function R and the fiber orientation distribution function S_δ.

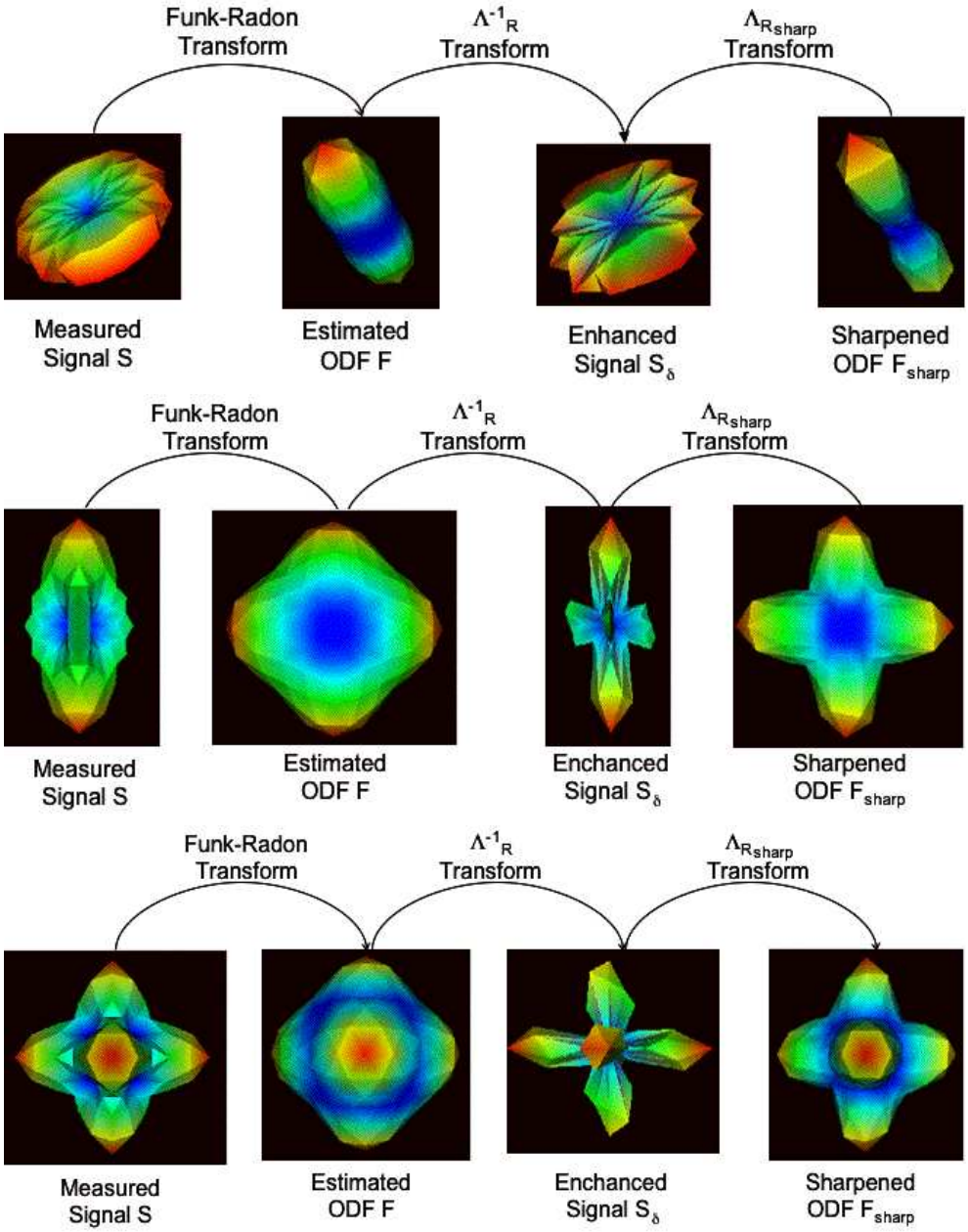

Figure 6: Delta function transform (DFT) sharpening illustration for 1, 2 and 3 fiber distributions.

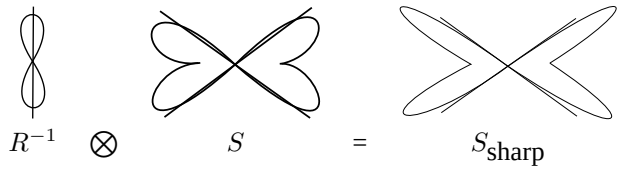

Figure 7: Rough sketch of the convolution of the inverse fiber response function R^{-1} and the measured signal S results in an enhanced signal S_{sharp}.

function S_δ. As described in [35], this convolution is a matrix multiplication when parameterizing the spherical functions with spherical harmonics expressed as

$$S = R \cdot S_\delta. \tag{23}$$

Hence, the product of the inverse fiber response function and the measured signal, i.e. $R^{-1} \cdot S$, mathematically gives S_δ but can also be viewed as a convolution in q-space. This intermediate convolution is illustrated in Fig. 7. We see that $R^{-1} \bigotimes S$ enhances the input signal. It can be interpreted as the signal that would have been generated assuming Gaussian fibers for the particular fiber distribution S_δ. This explains why the inverse DFT applied on the ODF gives a sharp version of the input signal.

Therefore, in our sharpening procedure, the inverse DFT is first applied to obtain an intermediate sharper version of the input signal and then the DFT is used to transform that enhanced signal into the desired sharp ODF using response functions $R(t)$ and $R_{\text{sharp}}(t)$ respectively. Note that the sharpening can be done differently by first applying the DFT with a sharp response, R_{sharp}, on the measured ODF and then compute the ODF with our standard matrix multiplication P of Eq. 19. Both methods require two linear transformations and we found differences between the two methods to be negligible. Hence, we decide not to mix transformations and we deal only with the DFT.

In summary, we use a series of two consecutive DFT-based linear transforms. Assuming the ODF is parametrized by the SH coefficients vector C, we first apply the inverse DFT with $R(t)$ to obtain the enhanced delta function signal coefficients and then apply the DFT with R_{sharp} to obtain the sharpened ODF coefficients, C_{sharp}, i.e.

$$C_{\text{sharp}} = \Lambda_{R_{\text{sharp}}} \cdot \Lambda_R^{-1} \cdot C$$

The procedure is clearly illustrated in Fig. 6 for 1, 2 and 3 fibers.

6 Results

In this section, we tested the effects of the b-value, the signal to noise ratio (SNR) in the signal generation, the approximation order ℓ of the SH series and the sharpening on the shape of the ODF estimated from synthetic and real data. We are both interested in the shape of the ODF as well as

the ability to extract local orientations from it with a very simple local maxima extraction procedure. First, every point on the normalized ODF surface mesh with a value above a threshold of 0.5 is a possible maxima *candidate*. Then, for each candidate, we look at its neighbors on the discrete sphere and look if their values are lower than its value. If so, the direction corresponding to the candidate gives a fiber orientation. This method is obviously very local and sensitive to noise but enough to illustrate the important and different characteristics of the estimated ODF. One can imagine more intelligent methods based on zero-crossings of the gradient or other computer vision based methods.

In all coming figures, the ODFs are stretched with respect to the surface values and should be viewed in color for a much clearer description. The color map is red for high values and blue for low values. When directions are overlaid, the thin green lines correspond to the ground truth fibers and the thicker yellow lines are the detected fibers.

6.1 Synthetic Data Experiment

As before, we randomly generate voxels with 1, 2 and 3 fibers using the multi-tensor Eq. 20. Using an order 3 tessellation, the angle between discrete mesh samplings is 16°. Considering noise and the known angular resolution limitation of the Gaussian fiber, we impose a minimum angle between fibers of 45°. We also require the fiber magnitudes (the p_k's in Eq. 20) to be random but between 0.3 and 0.7 for 2-fiber distributions and between 0.2 and 0.4 for 3-fiber distributions. Otherwise, the fiber compartments are too weak to detect any fibers. We vary the SNR between very noisy and typical noise levels, $\zeta = 5, 10, 20, 35$. Finally, we use b-values between 500, 1000, 2000, 3000, and 4000.

As mentioned earlier, min-max normalization [38] and minimum inscribed sphere (MIS) subtraction (Fig. 8) [21] are normally used to increase visual contrast in most papers in the literature. We are not only interested in visual appearance of the ODF but want to investigate the effects of enhancing individual underlying fiber compartments in a voxel. In Fig. 9, we show a 1-fiber example of the possible normalization and sharpening methods. Fig 9 is an example where the angle error between true direction and the detected maximum of the ODF is 6.18° in all cases. Note that some sharpening techniques are more aggressive than others. We must determine when sharpening should be performed and which sharpening method is best when optimal parameters, α and k, are used.

Figure 8: Minimum Inscribed Sphere (MIS) subtraction [21].

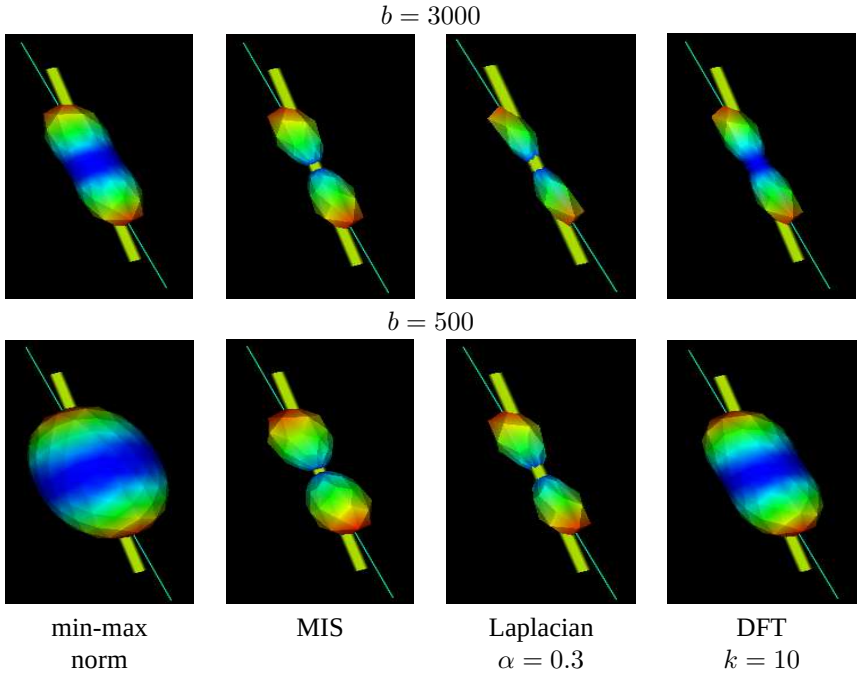

Figure 9: Normalization and sharpening methods for 1-fiber ODF examples.

6.1.1 Sharpening and Parameter Tests

We want to test which parameters give best orientation detection results from the estimated ODF. We must consider three things that directly influence the sharpening and ODF estimation: the b-value, the signal to noise ratio (SNR) and the SH series of order-ℓ used. The lower the b-value, the smaller the variance between fiber compartments and the harder it is to discriminate them. On the other hand, the lower the SNR, the more jagged and peaked the ODF and the higher the risk that sharpening will amplify and detect peaks due to noise. Hence, at low b-values and reasonable noise level, we expect that a more aggressive sharpening will perform better whereas a more conservative sharpening or none at all will perform best in the presence of noisy data. Finally, as described in [10], we have to take in to consideration that high order SH series approximations pick up the higher frequency modes of the signal and can thus be more sensitive to noise.

We perform tests for high b-values of 3000 and 4000 s/mm^2, for mid-range b-values of 1500 and 2000 and for low b-values of 500 and 1000. We also try high SNR of $\zeta = 35$, a mid-range SNR of $\zeta = 15$ and a low SNR of $\zeta = 5$. We adaptively modify the sharpening factors and truncation order of the spherical harmonics series to obtain the best maxima detection results. We have set $\lambda = 0.006$ based on the L-curves and simulations presented in [10]. From these tests, we observe consistent

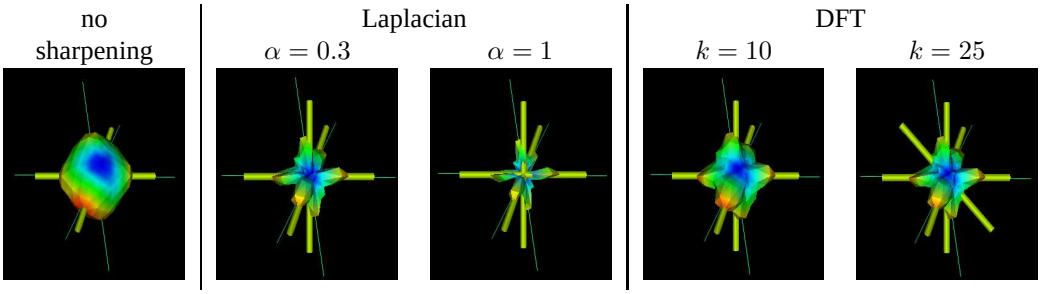

Figure 10: High quality diffusion signal of 3 fibers. SNR of $\zeta = 35$, fiber weights of $p_1 = 0.3$, $p_2 = 0.35$, $p_3 = 0.35$, smallest angle between fibers is $\theta = 57^\circ$ and $\ell = 8$ in SH series.

maxima detection behaviors independently of the b-values. That is, as expected, we have decreasing fiber detection results when the b-value is decreased but the other parameters have similar overall effects for all b-values. This is why we include quantitative results for only two b-values in Table 1. Information in that table can be summarized into three categories: 1) high, 2) average and 3) poor quality data. Figs. 10, 11, 12 are examples in each data category with a b-value of $b = 3000\text{s}/\text{mm}^2$. True fibers are the thin green lines and the detected ODF maxima are the thick yellow lines.

1. For high quality data, i.e low SNR $\zeta = 35$, the best results occur with a high truncation order $\ell = 8$ and conservative sharpening weight, $\alpha = 1$ and $k = 10$. This is because the signal is clean and unperturbed and thus we can catch the higher frequency modes of the spherical function and enhance the maxima without amplifying noise. A 3-fiber distribution example is shown in Fig. 10. We see that without sharpening, we underestimate the number of fibers by one and that if sharpening is too aggressive, we over estimate the number of fibers by one when $k = 30$.

2. For average quality data, i.e. SNR $\zeta = 15$, the best results occur when truncating the SH series at order $\ell = 6$ and with a moderate sharpening. It is not surprising that this is the case as an order-8 SH series models small variations due to noise and thus, overestimates the number of directions. This is illustrated in a 2-fiber distribution example in Fig. 11. The first row is for $\ell = 6$ and the second row is for $\ell = 8$ where we clearly see the over-modeling errors.

3. For poor quality data, i.e with high SNR of $\zeta = 5$, the best results are obtained for a smoother approximation with a low order $\ell = 4$. This gives a smoother ODF estimation and reduces the number overestimated fibers. Because the ODF is very smooth, one can then use an aggressive sharpening. We must keep in mind that current real data acquisition are rarely this noisy. We have included this test because it agrees with the expected hypothesis and illustrates the angular resolution limitations in the presence of noise with two fibers close to one another.

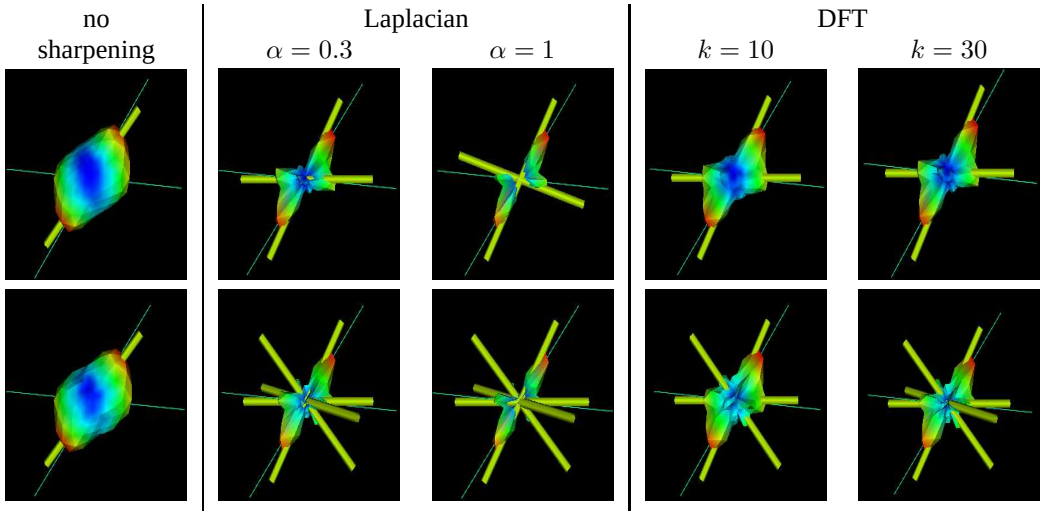

Figure 11: Average quality diffusion signal of 2 fibers. SNR of $\zeta = 15$, fiber weights of $p_1 = 0.42$, $p_2 = 0.58$, and $\theta = 55°$. First row is for a SH series of order $\ell = 6$ and second for $\ell = 8$.

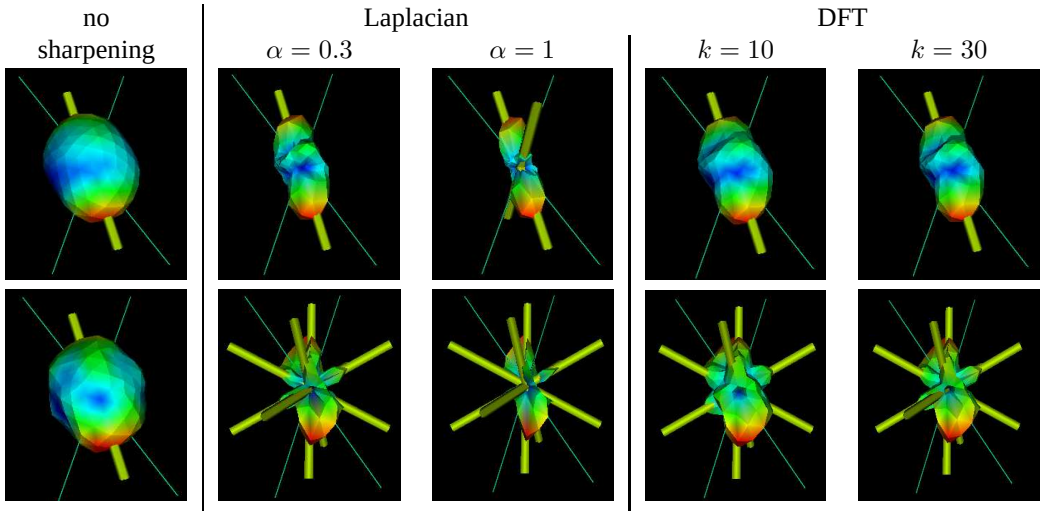

Figure 12: Poor quality image of two fibers close to one another. SNR of $\zeta = 5$, fiber weights of $p_1 = 0.43$, $p_2 = 0.57$ and $\theta = 51°$. The first row is for $\ell = 4$ and second for $\ell = 6$.

$b = 3000$		no sharp	Laplacian	DFT
$\zeta = 35$	$\ell = 8$	86.7%	99.1%, $\alpha = 1$	98.6%, $k = 10$
	$\ell = 6$	84.7%	98.2%, $\alpha = 5$	98.2%, $k = 30$
	$\ell = 4$	77.2%	88.0%, $\alpha = 10$	86.7%, $k = 200$
$\zeta = 15$	$\ell = 8$	87.0%	84.3%, $\alpha = 0.1$	90.8%, $k = 5$
	$\ell = 6$	84.2%	96.2%, $\alpha = 0.5$	96.3%, $k = 30$
	$\ell = 4$	75.9%	86.8%, $\alpha = 5$	84.8%, $k = 200$
$\zeta = 5$	$\ell = 8$	64.9%	—	—
	$\ell = 6$	78.5%	60.0%, $\alpha = 0.1$	71.7%, $k = 5$
	$\ell = 4$	75.5%	81.1%, $\alpha = 0.1$	80.9%, $k = 200$
$b = 1000$				
$\zeta = 35$	$\ell = 8$	65.1%	86.9%, $\alpha = 1$	82.3%, $k = 10$
	$\ell = 6$	64.1%	82.1%, $\alpha = 5$	79.6%, $k = 30$
	$\ell = 4$	62.4%	81.6%, $\alpha = 10$	75.8%, $k = 200$
$\zeta = 15$	$\ell = 8$	64.8%	56.5%, $\alpha = 0.1$	59.9%, $k = 5$
	$\ell = 6$	64.9%	85.0%, $\alpha = 0.5$	82.9%, $k = 30$
	$\ell = 4$	61.7%	80.5%, $\alpha = 10$	74.9%, $k = 200$
$\zeta = 5$	$\ell = 8$	65.0%	—	—
	$\ell = 6$	63.7%	58.4%, $\alpha = 0.1$	76.2%, $k = 5$
	$\ell = 4$	60.5%	81.6%, $\alpha = 0.1$	79.4%, $k = 200$

Table 1: Fiber detection results for $b = 3000, 1000\,\mathrm{s/mm^2}$ when varying SNR ζ, SH series order ℓ and sharpening weights α and k. For clarity, we only show results for best sharpening weight. — is when sharpening was not computed because ODF surface was too noisy.

These three categories are interpreted from results shown in Table 1. For clarity, we only show percentage success of the fiber detection for best sharpening weight and we choose not to show the exact number of underestimated and overestimated fibers, otherwise tables are too dense and unreadable. Without sharpening, we usually underestimate the true number of fibers (some ODF maxima are missed) unless we have high quality data and fibers are separated by a high angle. On the other hand, results also show that for a given truncation order, increasing the sharpening factor generally overestimates the data by creating maxima that amplify noise or small perturbations. Moreover, for low order truncation order, the estimation is usually relatively smooth so that sharpening cannot overestimate the estimation and thus, aggressive sharpening can greatly reduce the number of underestimated fibers. The right balance between truncation order and sharpening factor is highly dependent on the data and is well summarized in points 1), 2) and 3) above. This suggests that it is worth knowing the quality of the data and select accordingly the parameter before blindly estimating and sharpening the ODF.

It is also important to observe that for best SH order and sharpening weight selected, sharpening improves the fiber detection. In particular, for $b = 3000\,\mathrm{s/mm^2}$ and $\zeta = 15-35$, which are in ranges

of typical real data acquisition parameters, we have above 95% characterization rate with sharpening compared to around 87% without sharpening. The majority of the errors occur for fiber distributions where fibers are separated by 55° or less and have different relative weights. Considering noise and b-values, these cases are very hard to separate because of partial volume averaging. As we will see in the next section, voxels with fibers well separated at angles $> 60^\circ$, are much easier to distinguish. Overall, although not shown in the table, we recorded an average angle error of 11° between the ground truth and detected orientations. This is less than an angular step in our tessellation. Finally, from figures and tables, we note that the Laplacian enhancement produces sharper ODF shapes and slightly better fiber detection percentages than the DFT approach. This is not necessarily expected as the Gaussian fiber response function used in the DFT method actually agrees with the Gaussian fibers generated by the multi-tensor model. It shows that the Laplacian sharpening from the image processing is slightly more robust in the presence of noise. It also has the advantage of being model-free and faster to compute.

6.1.2 Considering Voxels With Isotropic Diffusion

Before attempting to process fields of real data, we must first explore the case when we have voxels with isotropic diffusion signal. In this case, we certainly do not want to sharpen or try to extract the ODF maxima. In [10], we showed that it was possible to use the generalized anisotropy (GA) [24] or the CRE [28] high order measures to differentiate isotropic, 1-fiber and multi-fiber distributions based on the estimation of the diffusion profile. However, these measures are ADC-based and in this work, we would like to use an ODF-based high order anisotropy measure to filter out isotropic diffusion voxels.

Tuch [38] defined the Generalized Fractional Anisotropy (GFA) as

$$GFA = \frac{\text{std}(ODF)}{\text{rms}(ODF)} = \sqrt{\frac{n_s \sum_{i=1}^{n_s} (\Psi(\mathbf{u}_i) - \langle\Psi\rangle)}{(n-1)\sum_{i=1}^{n_s} \Psi(\mathbf{u}_i)^2}},$$

which is the ratio of the standard deviation (std) and the root mean square (rms) of the ODF, where Ψ is the measured ODF, $\langle\Psi\rangle$ is the mean value on the ODF surface and $\mathbf{u}_i$ are all discrete directions on the sphere. This is a high order generalization of the classical FA measure which can similarly be defined as FA = std(σ) / rms(λ) [38, Appendix B], where σ are the eigenvalues of the diffusion tensor. As seen in Table 2, the measure is able to distinguish, 0, 1 and 2-fiber distributions reliably but in the case of noisy 3-fiber distributions, there is overlap in GFA values. For $b = 3000$ and a low SNR of $\zeta = 5$, we are no longer able to clearly discriminate isotropic and 3-fiber diffusion processes. This is less the case for low b-values, where noise is weighted down by the low frequency modes of the signal. This confirms that the signal is more vulnerable to noise for high b-values.

6.1.3 Field of Synthetic Data

We can now use GFA to set thresholds and filter out isotropic diffusion voxels, as done in DTI with the FA measure, before sharpening and extracting maxima of the ODF. Repeating the ODF fiber detection tests of the last section with isotropic, 1, 2 and 3 fiber distributions gives very similar

signal parameters		1 fiber	2 fibers	3 fibers	isotropic
$b = 3000$	$\zeta = 35$	0.34 ± 0.004	0.23 ± 0.02	0.16 ± 0.03	0.03 ± 0.005
	$\zeta = 15$	0.29 ± 0.008	0.21 ± 0.02	0.15 ± 0.03	0.05 ± 0.01
	$\zeta = 5$	0.12 ± 0.01	0.11 ± 0.02	0.08 ± 0.02	0.06 ± 0.01
$b = 1500$	$\zeta = 35$	0.18 ± 0.002	0.12 ± 0.02	0.07 ± 0.02	0.007 ± 0.001
	$\zeta = 15$	0.18 ± 0.005	0.11 ± 0.02	0.07 ± 0.02	0.02 ± 0.003
	$\zeta = 5$	0.15 ± 0.01	0.11 ± 0.02	0.08 ± 0.02	0.04 ± 0.01
$b = 500$	$\zeta = 35$	0.10 ± 0.002	0.06 ± 0.008	0.04 ± 0.009	0.005 ± 0.001
	$\zeta = 15$	0.10 ± 0.004	0.06 ± 0.009	0.04 ± 0.010	0.01 ± 0.002
	$\zeta = 5$	0.09 ± 0.01	0.07 ± 0.01	0.05 ± 0.01	0.03 ± 0.006

Table 2: Mean and standard deviation GFA over 10000 ODF estimations from 0-, 1-, 2- and 3-fiber diffusion signals. For noisy, average and high quality data we use a SH series estimation of $\ell = 4$, 6, 8 respectively. There is overlap in GFA values between 3-fiber and isotropic columns for $\zeta = 5$.

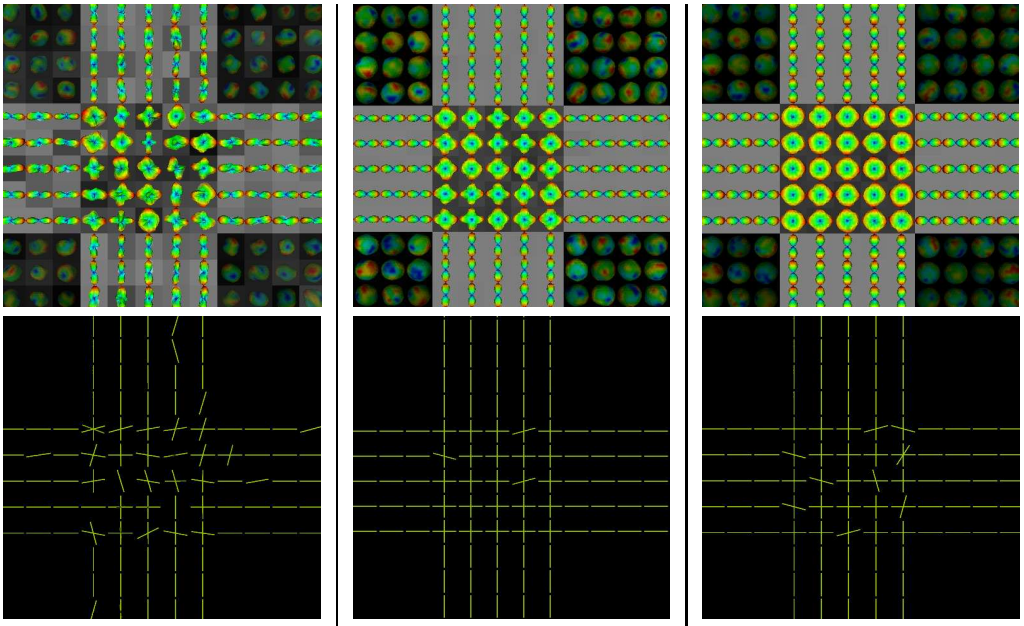

$b = 3000, \zeta = 5, \ell = 4$ | $b = 1500, \zeta = 15, \ell = 6$ | $b = 500, \zeta = 35, \ell = 8$

Figure 13: 90° crossing distributions. Sharpening is not necessary for perpendicular fibers.

results and leads to the same conclusion as above. We do not include a new set of tables here but instead show representative examples in Figs. 13 and 14.

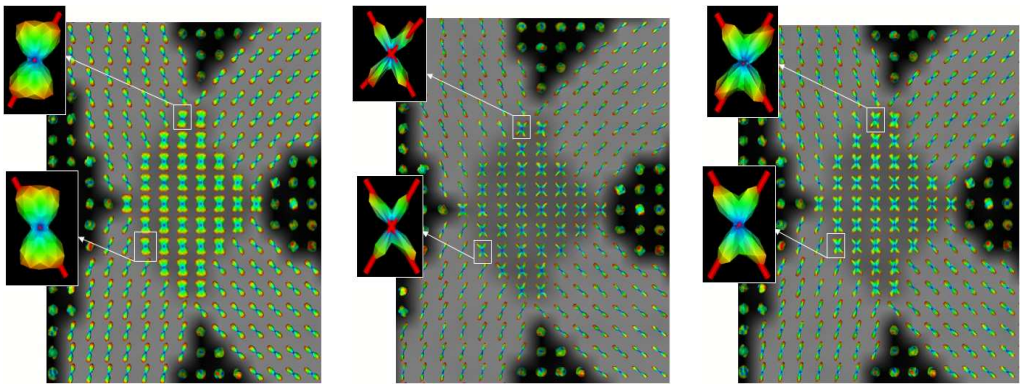

No sharp Laplacian, $\alpha = 1$ DFT, $k = 30$

Figure 14: SNR $\zeta = 15$, $b = 1500$, $\ell = 6$. $\theta = 55^\circ$ between fiber bundles. Sharpening improves fiber detection in voxels high-lighted with boxes.

First, we illustrate what happens when 2 synthetic fibers cross at 90° angles for three different examples with different SNR and b-values. Column 1 and 3 of Fig. 13 represent difficult datasets because the input signal is either very noisy or very smooth and spherical (low b-value), which makes the fiber extraction more sensitive than for in-between parameters used in column 2. Based on Table 1, we have used an order 4, 6 and 8 SH series respectively. Note that in both cases, we are able to characterize the fiber crossing regions and filter out isotropic voxels in the background. Due to the simpler nature of perpendicular fibers, the ODF maxima agree relatively well with the underlying fiber orientations. Hence, we do not need sharpening in this case. As seen in Fig. 14, fiber detection is improved with sharpening when there are more complicated configurations of fibers with smaller angles between crossings. The two fiber bundles are intersecting at angles of 55°. We have generated an average quality dataset with SNR of $\zeta = 15$ and b-value of 1500 $\mathrm{s/mm^2}$. In this example, we can see the usefulness of sharpening in voxels of the crossing. Some fibers are missed from the un-sharp ODF whereas the maxima are much clearer when we add sharpening.

6.2 Biological Phantom Experiment

We test our algorithm on a biological phantom produced by Campbell et al. at the McConnel Brain Imaging Center and Montreal Neurological Institute [6, 7] and was created from two excised Sprague-Dawley rat spinal cords embedded in 2% agar. A high angular resolution dataset was acquired using 90 gradient directions with $b = 3000$ $\mathrm{s/mm^2}$. The baseline T1-weighted image illustrating the ground truth configurations of the fibers is seen in the top left of Fig. 15. The crossing regions is high-lighted and we have chosen to visualize the slice where there is partial volume averaging due to the fiber bundles passing through the crossing voxels. In the first row of Fig. 15, we also include the FA and GFA anisotropy measures as well as the DTI ellipsoid surfaces obtained from

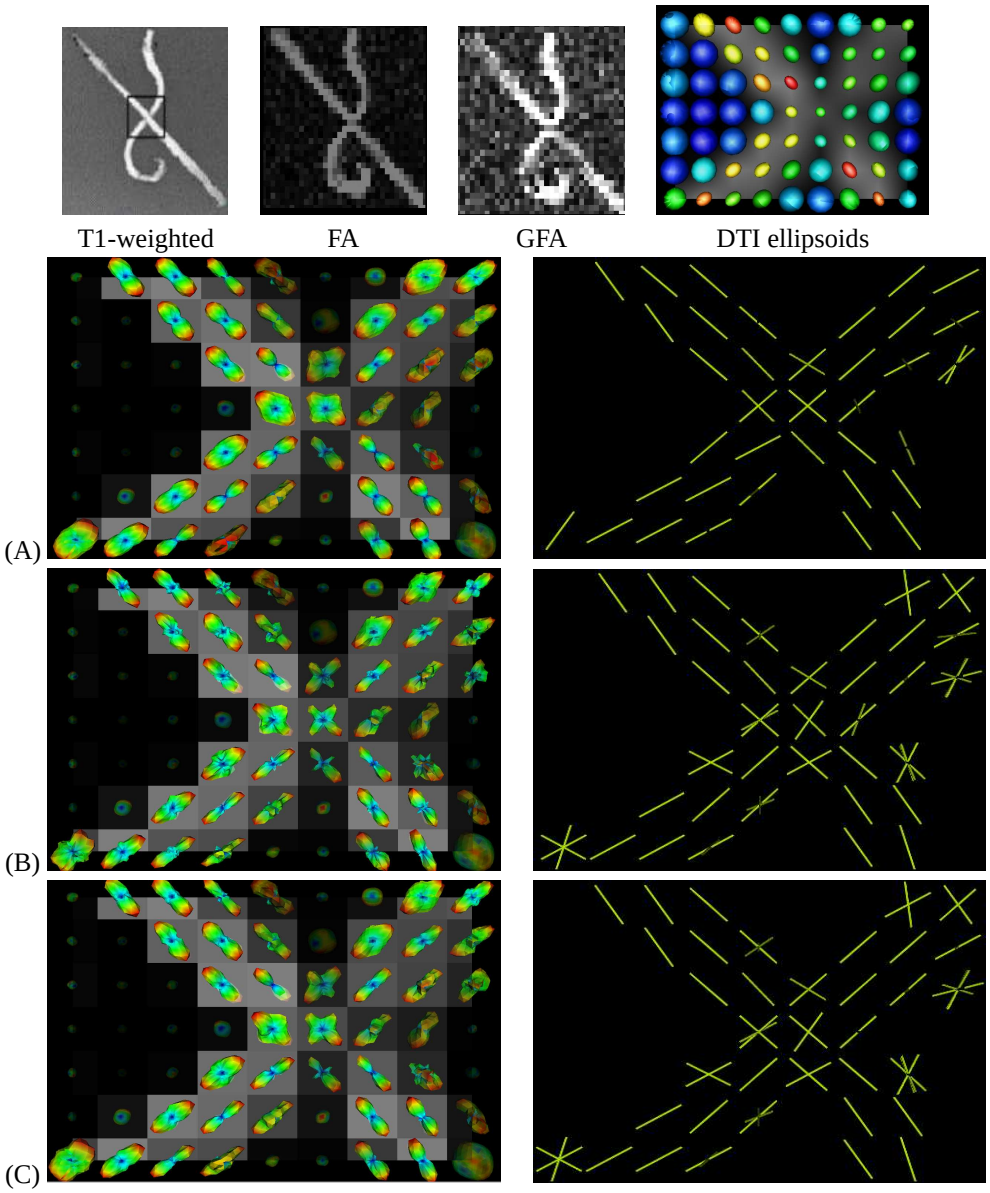

Figure 15: Results for the rat biological phantom from Campbell et al. [7]. (A) is without sharpening, (B) is with Laplacian $\alpha = 0.5$ and (C) is with DFT $k = 10$ sharpening.

the standard DTI least-squares fit using all 90 directions. As expected, the DTI ellipsoid surfaces are planar and tend to be spherical in the crossing area which results in ambiguous principal directions.

Since the rat data set has a b-value of 3000 s/mm^2 and is quite noisy, as seen in the FA and GFA maps, we have decided to use an order-6 SH series estimation with conservative sharpening factors. We visualize the field of ODFs by adjusting the opacity of each surface with respect to the GFA measure and sharp and extract ODF maxima only for voxels above a certain GFA measure. We see that ODFs in the crossing region have two strong peaks that we reliably recover. Since fibers are perpendicular, sharpening enhances the overall ODF shapes but does not greatly improve the maxima detection procedure. Although it is recovering an extra 2-fiber orientation voxel at the bottom of the crossing section, it is also creating local maxima at boundaries between rat chords and background substance where the noise is more important. Nonetheless, sharpening seems to improve the general shape of the ODFs which could potentially better direct tractography methods based on the full ODF. Overall, the shape of the ODFs are very satisfying and qualitatively seem to better describe the underlying fibers than the ODFs reported in [7, 29]. It would now be interesting to compare our estimated directions with the estimated ground truth and regularized directions of Savadjiev et al. presented in [29].

6.3 Human Brain Data Experiment

We finally test our method on a real human brain dataset. Diffusion weighted images were acquired at the Center for Magnetic Resonance Research, University of Minnesota, on a 3 Tesla Siemens Magneton Trio whole-body scanner. We used 81 gradient directions on the hemisphere with 3 repetitions per direction, each with a b-value of $b = 1000\ s/mm^2$, $TR = 5100s$ and $TE = 109ms$. The voxel size was a $3mm^3$ cube and there were 24, 64x64 slices. We illustrate our ODF estimation and sharpening on three regions of interests (ROI) in the brain, Figs. 16, 17 and 18. For all, we use a SH series of order 6 and conservative sharpening factors. As before, we high-light the region of interest and compute the least-squares DTI ellipsoids.

The first ROI is in an axial slice showing the intersection between the splenium of the corpus callosum and the optic radiation. This slice is taken towards the back of the head and corresponds to the ROI of Tuch [38, Fig.7]. Note that we pick up all three main fiber bundles as well as multiple fiber voxels where we detect directions going up towards the top of the brain (splenium branching upwards). Since the $b = 1000$ s/mm^2 is a low b-value, we see the improvement brought by sharpening.

The second ROI is a coronal slice of the intersection between transcallosal projections of the body of the corpus callosum, the corona radiata and the superior longitudinal fasciculus. This is a very similar region as the ROIs in the centrum semiovale of [40] and [35]. We see two important crossings. First, the corona radiata crossing the transcallosal fibers projecting to the precentral gyrus and secondly, we have high-lighted the crossings between transcallosal projections and superior longitudinal fasciculus. The superior longitudinal fibers are harder to see as they come out of the page. This is also the case for the corpus callosum body coming out of the page as well in the lower left corner. Note the positive effects of sharpening the ODFs in the crossing areas.

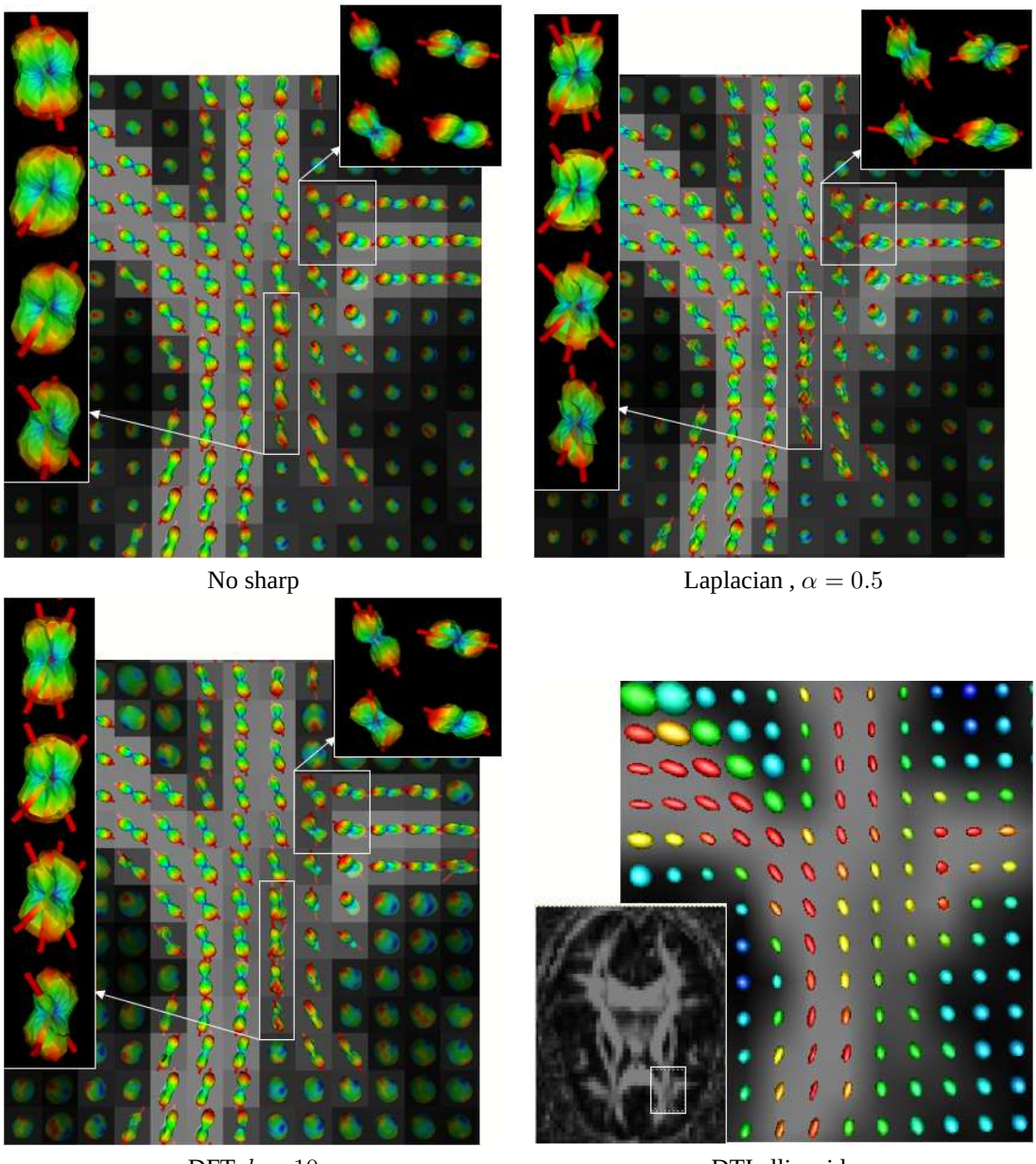

Figure 16: Axial slice showing intersection between the splenium of the corpus callosum, the tapetum and optic radiation such as the one in [38].

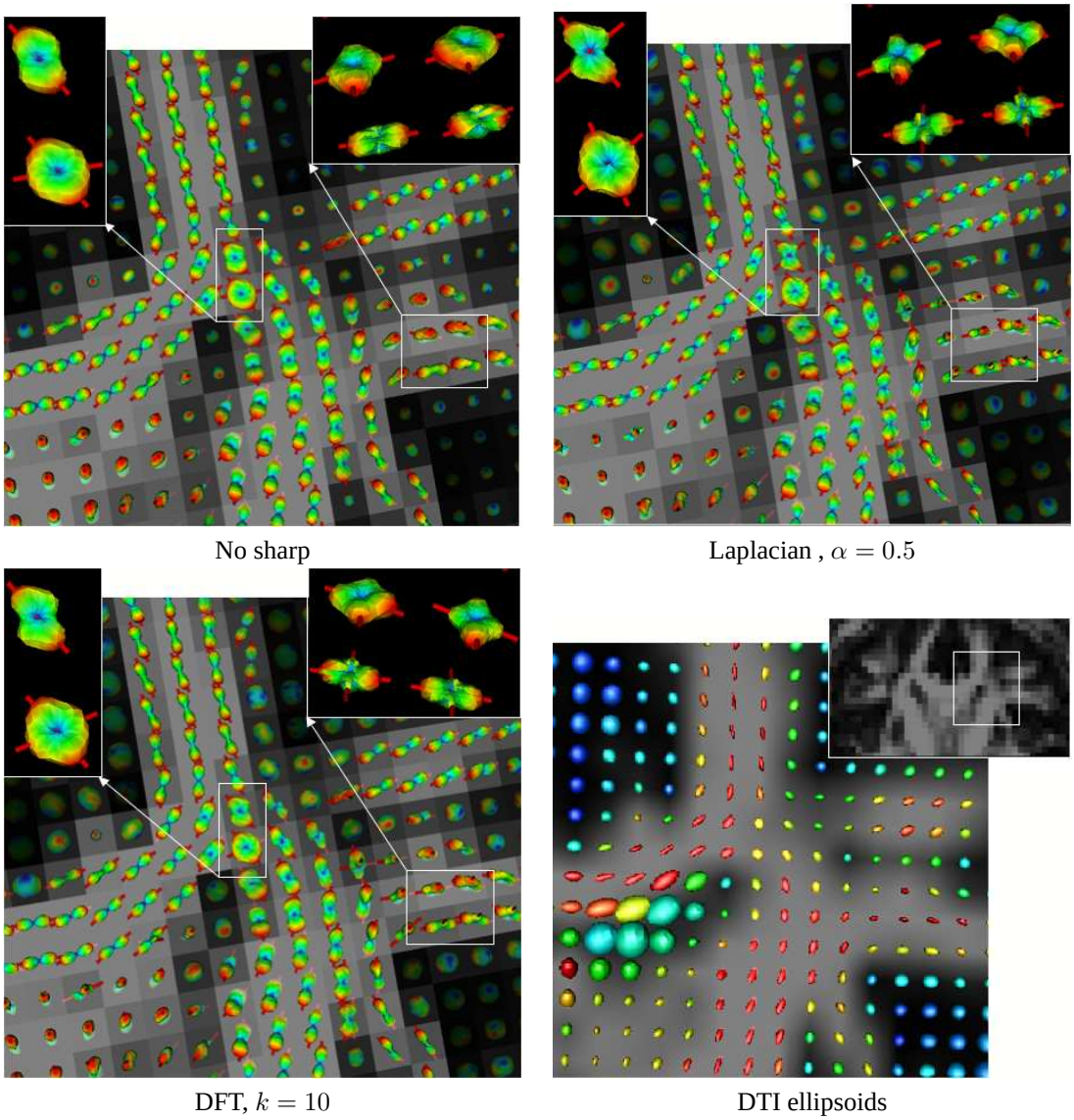

Figure 17: Coronal slice in the centrum semiovale. We see intersection between the corpus callosum commisural fibers and the corona radiata and superior longitudinal fasciculus.

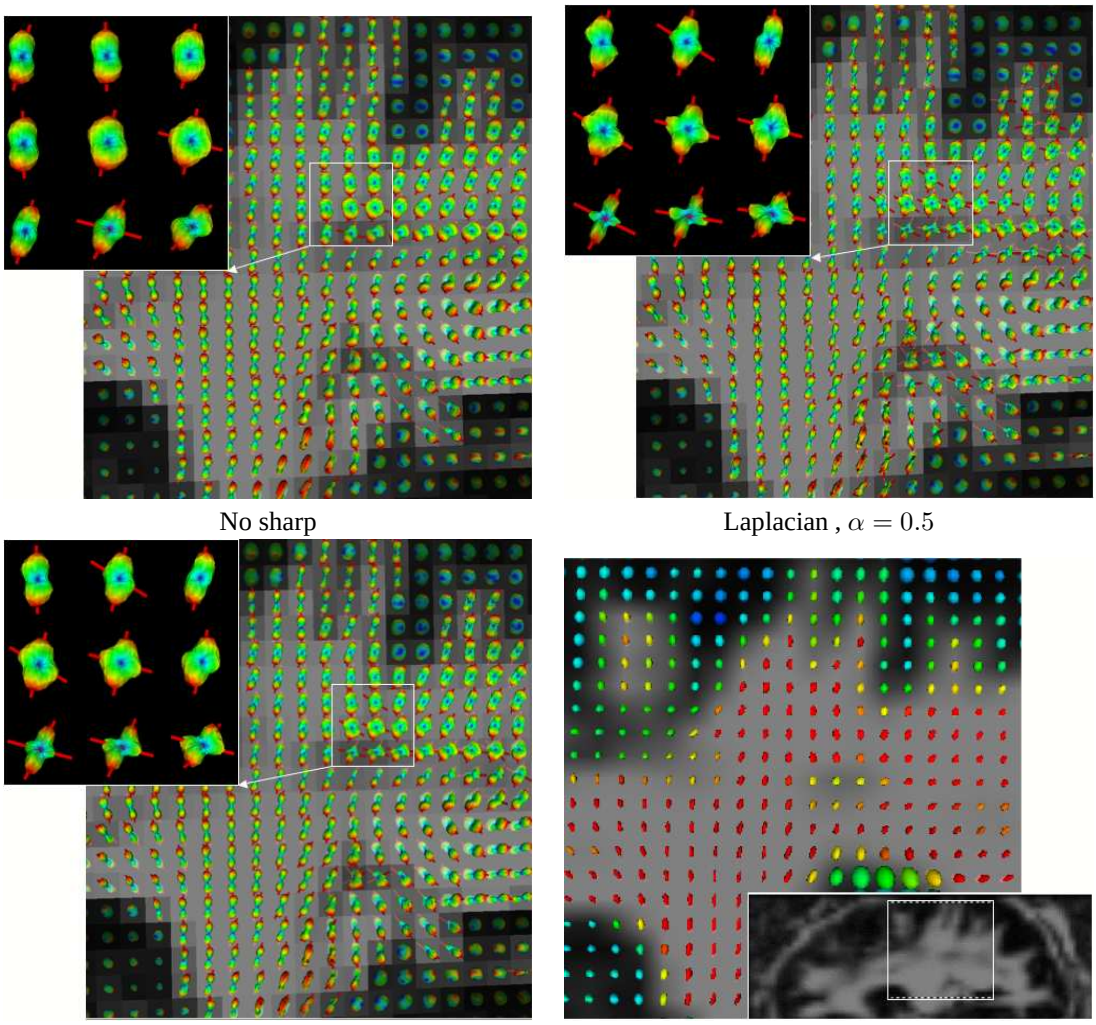

Figure 18: Sagittal slice showing the corona radiata diverging fibers and crossings with the longitudinal fasciculus.

Finally, we show a sagittal slice taken in the corona radiata showing diverging and crossing fibers. We detect multiple fibers towards the top right of the brain. Some crossings are due to diverging and splitting fibers in the corona radiata. There are also crossings between the corona radiata and the superior longitudinal fasciculus (left-right) fibers that appear and are much clearer with sharpening.

7 Discussion

It is important to discuss the recent paper by Ozarslan et al. [22] because it is in similar spirit as our approach. While we have extensively shown the power of SH series to simplify integrals over the sphere using the Funk-Hecke formula, Ozarslan et al. also uses a SH series approximation to obtain an analytic solution of the original Fourier integral of Eq. 1 under mono-exponential assumption. In particular, [22] and their more detailed technical report [23] describes how to find the diffusion orientation transform (DOT) that takes the apparent diffusion profile (D in Eq. 2) to the diffusion probability profile (PDF) (P in Eq. 1). The key idea is to note that the Fourier transform can be done using the Rayleigh expansion of a plane wave in spherical coordinates. They had previously used this in [25] but now find an analytic solution using a spherical harmonics approximation to obtain the closed form expression based on the confluent hypergeometic function [22]. The DOT has the advantage of being based on the exact PDF of Eq. 1 in which a general ℓ-order Bessel function appears whereas ODF-based reconstruction methods using the Funk-Radon transform approximation have an intrinsic zeroth-order Bessel function smoothing. However, for simplification, they use a {mono,bi,tri}-exponential decay of the input signal to obtain the diffusion profile [23] whereas in our case, we have a model-free approach. Hence, there is a trade-off between a simple analytic expression for an approximation of the ODF and a more complicated analytic solution for the exact PDF based on the an exponential decay assumption. This monoexponential assumption can be seen as a low-pass filtering of the diffusion PDF. Which method is more efficient and more precise needs to be explored in future work in order to determine which is more useful in practice.

8 Conclusion

There are several important contributions in this paper. First, we have derived an analytic solution of the Funk-Radon transform commonly solved numerically in Q-ball reconstruction to estimate the orientation distribution function (ODF). This was possible using a physically meaningful spherical harmonics approximation of the measured signal. The final ODF estimation is an elegant product of the modified spherical harmonic basis function with the simple ratio of the corresponding order-ℓ Legendre polynomials evaluated at 0 and at 1. This simplification was possible by using a delta sequence of Gaussians with decreasing variance so that the Funk-Hecke formula could be used to solve the Funk-Radon integral. Without this derivation, the FRT can only be computed with a more complicated numerical scheme.

We have also thoroughly tested the ODF estimation and have shown its robustness and flexibility. It is clear that multiple fiber distributions can be detected from noisy sparse data with different imaging parameters. In particular, we have illustrated that the b-value, the signal to noise ratio

(SNR) and the approximation order-ℓ of the SH series affect the orientation procedure. A priori, the lower the b-value, the harder the fiber compartments are to separate. Hence, the ODFs are much sharper and easier to characterize into different fiber compartments for high b-value than low b-value where the signal tends to be more isotropic. Furthermore, the higher the SNR, the less risk there is to overestimate the fiber distribution with a SH series of high order-8. In the case of an average quality data, truncation at order-6 performs best. It is worth mentioning that it is also possible to obtain very similar results by always using the highest possible truncation order ($\ell = 8$) but using a higher λ regularization parameter. However, since order 8, 6 and 4 respectively have 45, 21 and 15 SH coefficients, the ODF estimation is computationally more expensive for large volumes. It will be part of future work to investigate the precise relation between truncation order ℓ and the smoothing parameter λ. It could also be important to explore dynamic truncation schemes as suggested by Alexander et al. [2].

Finally, in this paper, we have chosen to focus on the individual ODF shapes before attempting any tractography and segmentation. We observed that in most cases, once the isotropic diffusion voxels have been filtered out, ODF sharpening seems important and we have shown that it enhances the overall shape and underlying fiber distribution without dramatically amplifying the noise level. To our knowledge, this is the first attempt at studying ODF shape enhancement. We have defined a Laplacian-based image processing approach and a delta function transform (DFT) inspired by spherical deconvolution. Even though the DFT is elegant and uses some interesting ideas and properties of spherical harmonics, it needs to assume a fiber response function. It is not as robust as the model-free Laplace-Beltrami sharpening which is also faster to compute. It is clear that we now have to thoroughly test if sharpening the overall shape of the ODF leads to better tractography and segmentation results.

Acknowledgments

The authors would like to thank the McConnel Brain Imaging Center (BIC) of McGill University and especially, J. Campbell, K. Siddiqi, P. Savadjiev, V. V. Rymar and B. Pike for the rat cord dataset. This exchange was supported by the FFCR grant, the CRSNG Canada graduate scholarship and INRIA International internships program. Morever, thanks to S. Lehéricy and K. Ugurbil at the Center for Magnetic Resonance Research at the Minnesota University for the high angular human brain dataset. This part was partially supported by grants NSF-INRIA Cooperative Research. The authors would like to thank Martin de La Gorce and Christophge Lenglet for useful discussion and valuable inputs.

References

[1] D. C. Alexander. Maximum entropy spherical deconvolution for diffusion mri. In *Image Processing in Medical Imaging*, pages 76–87, 2005.

[2] D.C. Alexander, G.J. Barker, and S.R. Arridge. Detection and modeling of non-gaussian apparent diffusion coefficient profiles in human brain data. *Magn Reson Med*, 48:331–340, 2002.

[3] G.E. Andrews, R. Askey, and R. Roy. *Special Functions*. Cambridge University Press, 1999.

[4] P.j. Basser, J. Mattiello, and D. LeBihan. MR diffusion tensor spectroscopy and imaging. *Biophysical Journal*, (66):259–267, 1994.

[5] T.E.J. Behrens, M.W. Woolrich, M. Jenkinson, H. Johansen-Berg, R.G. Nunes, S. Clare, P.M. Matthews, J.M. Brady, and S.M. Smith. Characterization and propagation of uncertainty in diffusion-weighted mr imaging. *Magn Reson Med*, 50:1077–1088, 2003.

[6] J. Campbell. *Diffusion Imaging of White Matter Fiber Tracts*. PhD thesis, McGill University, 2004.

[7] S.W. Campbell, K. Siddiqi, V.V. Rymar, A.F. Sadikot, and G.B. Pike. Flow-based fiber tracking with diffusion tensor q-ball data: Validation and comparison to principal diffusion direction techniques. *NeuroImage*, 27(4):725–736, October 2005.

[8] Y. Chen, W. Guo, Q. Zeng, G. He, B.C. Vemuri, and Y. Liu. Recovery of intra-voxel structure from hard dwi. In *ISBI*, pages 1028–1031. IEEE, 2004.

[9] Y. Chen, W. Guo, Q. Zeng, X. Yan, F. Huang, H. Zhang, G. He, B.C. Vemuri, and Y. Liu. Estimation, smoothing, and characterization of apparent diffusion coefficient profiles from high angular resolution dwi. In *Computer Vision and Pattern Recognition*, volume 1, pages 588–593, July 2004.

[10] M. Descoteaux, E. Angelino, S. Fitzgibbons, and R. Deriche. Apparent diffusion coefficients from high angular resolution diffusion imaging: Estimation and applications. Technical Report 5681, INRIA, September 2005.

[11] L.R. Frank. Anisotropy in high angular resolution diffusion-weighted mri. *Magn Reson Med*, 45:935–939, 2001.

[12] L.R. Frank. Characterization of anisotropy in high angular resolution diffusion-weighted mri. *Magn. Res. Med*, 47:1083–1099, 2002.

[13] P.C. Hansen. The l-curve and its use in the numerical treatment of inverse problems. In P. Johnston, editor, *Computational Inverse Problems in Electrocardiology,*, pages 119–142, 2001.

[14] M. Lazar, D.M. Weinstein, J.S. Tsuruda, K.M. Hasan, K. Arfanakis, M.E. Meyerand, B. Badie, H.A. Rowley, V.Haughton, A. Field, and A.L. Alexander. White matter tractography using diffusion tensor deflection. In *Human Brain Mapping*, volume 18, pages 306–321, 2003.

[15] D. LeBihan, E. Breton, D. Lallemand, P. Grenier, E. Cabanis, and M. Laval-Jeantet. MR imaging of intravoxel incoherent motions: Application to diffusion and perfusion in neurologic disorders. *Radiology*, pages 401–407, 1986.

[16] C. Lenglet, M. Rousson, R. Deriche, and O. Faugeras. Statistics on the manifold of multivariate normal distributions: Theory and application to diffsuion tensor mri. *Journal of Mathematical Imaging and Vision, Special Issue MIA'04*, 2005, in press.

[17] C. Lenglet, M. Rousson, R. Deriche, O. Faugeras, S. Lehericy, and K. Ugurbil. A riemannian approach to diffusion tensor images segmentation. In *Information Processing in Medical Imaging*, pages 591–602, 2005.

[18] C.P. Lin, V.J. Wedeen, J.H. Chen, C. Yao, and W.Y. I. Tseng. Validation of diffusion spectrum magnetic resonance imaging with manganese-enhanced rat optic tracts and ex vivo phantoms. *NeuroImage*, 19:482–495, 2003.

[19] C. Liu, R. Bammer, and M.E. Moseley. Limitations of apparent diffusion coefficient-based models in characterizing non-gaussian diffusion. *Magn Reson Med*, 54:419–428, 2005.

[20] K. M.Jansons and D. C.Alexander. Persistent angular structure: new insights fom diffusion magnetic resonance imaging data. *Inverse Problems*, 19:1031–1046, 2003.

[21] E. Ozarslan and T. Mareci. Generalized diffusion tensor imaging and analytical relationships between diffusion tensor imaging and high angular resolution imaging. *Magn Reson Med*, 50:955–965, 2003.

[22] E. Ozarslan, T.M. Shepherd, B.C. Vemuri, S.J. Blackband, and T.H. Mareci. Fast orientation mapping from hardi. In *MICCAI*, volume 3749, pages 156–163, 2005.

[23] E. Ozarslan, T.M. Shepherd, B.C. Vemuri, S.J. Blackband, and T.H. Mareci. Resolution of complex tissue microarchitecture using the diffusion orientation transform (dot). Technical Report TR05-004, University of Florida, July 2005.

[24] E. Ozarslan, B. Vemuri, and T. Mareci. Generalized scalar measures for diffusion mri using trace, variance and entropy. *Magn Reson Med*, 53:866–876, 2005.

[25] E. Ozarslan, B. C. Vemuri, and T. Mareci. Fiber orientation mapping using generalized diffusion tensor imaging. In *ISBI*, pages 1036–1039, 2004.

[26] M. Perrin, C. Poupon, Y. Cointepas, B. Rieul, N. Golestani, C. Pallier, D. Riviere, A. Constantinesco, D. Le Bihan, and J.-F. Mangin. Fiber tracking in q-ball fields using regularized particle trajectories. In *Information Processing in Medical Imaging*, pages 52–63, 2005.

[27] C. Poupon. *Détection des faisceaux de fibres de la substance blanche pour l'étude de la connectivité anatomique cérébrale.* PhD thesis, Ecole Nationale Supérieure des Télécommunications, December 1999.

[28] M. Rao, Y. Chen, B.C. Vemuri, and F. Wang. Cumulative residual entropy: A new measure of information. *IEEE Transactions on Information Theory*, 50:1220–1228, 2004.

[29] P. Savadjiev, J.S.W. Campbell, G.B. Pike, and K. Siddiqi. 3d curve inference for diffusion mri regularization. In *MICCAI*, volume 3749, pages 123–130, 2005.

[30] J. Sijbers, A. J. den Dekker, J. Van Audekerke, M. Verhoye, and D. Van Dyck. Estimation of the noise in magnitude mr images. *Magnetic Resonance Imaging*, 16(1):87–90, 1998.

[31] Jan Sijbers. *Signal and Noise Estimation from Magnetic Resonance Images*. PhD thesis, Universiteit Antwerpen, 1998.

[32] O. Soderman and B. Jonsson. Restricted diffusion in cylindrical geometry. *Journal Of Magnetic Resonance*, A(117):94–97, 1995.

[33] M.R. Spiegel and J. Liu. *Mathematical Handbook of Formulas and Tables*. Schaum's Outlines, 2nd edition, 1999.

[34] E.O. Stejskal and J.E. Tanner. Spin diffusion measurements: spin echoes in the presence of a time-dependent field gradient. *Journal of Chemical Physics*, 42:288–292, 1965.

[35] J.-D. Tournier, F. Calamante, D.G. Gadian, and A. Connelly. Direct estimation of the fiber orientation density function from diffusion-weighted mri data using spherical deconvolution. *NeuroImage*, 23:1176–1185, 2004.

[36] D. Tschumperlé and R. Deriche. Variational frameworks for DT-MRI estimation, regularization and visualization. In *Proceedings of the 9th International Conference on Computer Vision*, pages 116–121, Nice, France, 2003. IEEE Computer Society, IEEE Computer Society Press.

[37] D. Tuch. *Diffusion MRI of Complex Tissue Structure*. PhD thesis, Harvard University and Massachusetts Institute of Technology, 2002.

[38] D. Tuch. Q-ball imaging. *Magn Reson Med*, 52:1358–1372, 2004.

[39] D.S. Tuch, T.G. Reese, M.R. Wiegell, N.G. Makris, J.W. Belliveau, and V.J. Wedeen. High angular resolution diffusion imaging reveals intravoxel white matter fiber heterogeneity. *Magn. Res. Med.*, 48:577–582, 2002.

[40] D.S. Tuch, J.J. Wisco, M.H. Khachaturian, L.B. Ekstrom, R. Kotter, and W. Vanduffel. Q-ball imaging of macaque white matter architecture. *Philosophical Transactions of the Royal Society B*, 360:869–879, May 2005.

[41] Z. Wang, B.C. Vemuri, Y. Chen, and T. Mareci. Simultaneous smoothing and estimation of the tensor field from diffusion tensor mri. In *IEEE Conference on Computer Vision and Pattern Recognition*, volume I, pages 461–466, Madison, Wisconsin (United States), June 2003.

[42] V.J. Wedeen, T. G. Reese, D.S. Tuch, J.-G. Dou, R.M. Weiskoff, and D. Chessler. Mapping fiber orientation spectra in cerebral white matter with fourier-transform diffusion mri. In *Proceedings of the International Society for the Magnetic Resonance in Medecine*, page 321, 1999.

[43] C.F Westin, S.E Maier, H. Mamata, A. Nabavi, F.A. Jolesz, and R. Kikinis. Processing and visualization for diffusion tensor MRI. In *In proceedings of Medical Image Analysis*, volume 6(2), pages 93–108, 2002.

A Funk-Radon transform approximates the diffusion ODF

The proof in this section is more detailed and slightly different than the one published in [38, Appendix A]. Let $\mathcal{F}_{2D}$, $\mathcal{F}_{3D}$ and $\mathcal{G}$ represent the 2D Fourier, 3D Fourier and Funk-Radon (FRT) transforms respectively. We want to prove that the FRT approximates the ODF, $\mathcal{G}[S(\mathbf{q})](u) \approx \Psi(u)$. For this, it is worth stating important Fourier analysis tools required for the proof.

1. **Parseval-Plancherel Theorem** relates the integral of two functions over real space to the integral of their Fourier transforms over q-space as

$$\int_{-\infty}^{\infty} f(x)\bar{g}(x)dx = \int_{-\infty}^{\infty} F(k)\bar{G}(k)dk, \tag{24}$$

   where $F(k) \equiv \mathcal{F}[f(x)](k)$ and $\bar{g}$ is the complex conjugate of g.

2. The **Central Slice Theorem** states that the 2D Fourier transform of the projection of a function $f(x)$ onto the plane defined by the vector $\mathbf{u}$ is the same as the intersection of that plane with the 3D Fourier transform of $f(x)$. Letting $\mathbf{u}$ be a unit normal vector defining the projection plane and $\mathbf{x}$ a point on that plane, we can define the projection $\mathcal{L}$ of a 3D function $f(\mathbf{x})$ as

$$\mathcal{L}[f(\mathbf{x}))](\mathbf{u}) = \int_{-\infty}^{\infty} f(\mathbf{x} + \alpha\mathbf{u})d\alpha. \tag{25}$$

   Define now the intersection of a 3D function $f(\mathbf{x})$ with the plane defined by the normal vector $\mathbf{u}$ to it as $\mathcal{I}[f(\mathbf{x})](\mathbf{u}) = f(\mathbf{x})\delta(\mathbf{x}^T\mathbf{u})$, where δ is the Dirac delta function. Hence, we can formally write the central slice theorem as

$$\mathcal{F}_{2D}[\mathcal{L}[f(\mathbf{x})](\mathbf{u})] = \mathcal{I}[\mathcal{F}_{3D}[f(\mathbf{x})]](\mathbf{u}) \quad \text{or} \quad \mathcal{L}[f(\mathbf{x})](\mathbf{u})] = \mathcal{F}_{2D}[\mathcal{I}[\mathcal{F}_{3D}[f(\mathbf{x})]](\mathbf{u})] \tag{26}$$

   if f is antipodelly symmetric.

3. The **Hankel transform** $\mathcal{H}$ is a special case of the 2D Fourier transform of a function f when this function has no angular dependence, i.e. $f(x, y) = f(r)$ when written in polar coordinates. Letting $x = r\cos\theta$, $y = r\sin\theta$, $u = q\cos\phi$, $v = q\sin\phi$, we can derive the Hankel transform as

$$\begin{aligned}
\mathcal{F}_{2D}[f(x)] &= \int_{-\infty}^{\infty}\int_{-\infty}^{\infty} f(x,y)\exp\left(-2\pi i(ux+vy)\right)dxdy \\
&= \int_{0}^{\infty}\int_{0}^{2\pi} f(r)\exp\left(-2\pi iqr(\cos\theta\cos\phi+\sin\theta\sin\phi)\right)rdrd\theta \\
&= \int_{0}^{\infty}\int_{0}^{2\pi} f(r)\exp\left(-2\pi iqr\cos(\theta-\phi)\right)rdrd\theta \\
&= \int_{0}^{\infty} f(r)\left(\int_{0}^{2\pi}\exp(-2\pi iqr\cos\theta)d\theta\right)rdr \\
&= 2\pi\int_{0}^{\infty} f(r)J_0(2\pi qr)rdr \qquad \text{since } J_0(z) = \frac{1}{\pi}\int_{0}^{\pi}\exp(iz\cos\theta)d\theta \\
&= \mathcal{H}[f(x,y)]
\end{aligned} \tag{27}$$

We can now derive the relation between the ODF Ψ and Funk-Radon transform $\mathcal{G}$ of the measured signal $S(\mathbf{q})$. To do so, we express both functions in cylindrical coordinates (r, θ, z). Without loss of generality, the point of the unit sphere $\mathbf{u}$ where we want to evaluate the ODF given by Eq. 6 is along the z-axis. Thus, we first note that the ODF can be evaluated by first projecting the PDF onto the xy-plane and taking the value at the origin.

$$\begin{aligned}
\Psi(\mathbf{u}) &= \int_0^\infty P(\alpha \cdot \mathbf{u}) d\alpha \\
&= \mathcal{L}[P(0)](\mathbf{u}) \qquad \text{(using Eq.25)} \\
&= \int_{-\infty}^{\infty} P(0,0,z) dz \\
&= \int_{-\infty}^{\infty} \int_0^{2\pi} \int_0^\infty P(r,\theta,z)\delta(r,\theta) r dr d\theta dz
\end{aligned} \tag{28}$$

We now expend the FRT of the raw signal, $\mathcal{G}_{q'}[S(\mathbf{q})](\mathbf{u})$ and show that it approximates the ODF. First, since $\mathbf{u}$ is along the z-axis, the FRT in the direction $\mathbf{u}$ is integral over the great circle in the xy-plane, i.e.

$$\begin{aligned}
\mathcal{G}_{q'}[S(\mathbf{q})](\mathbf{u}) &= \int_0^{2\pi} S(q', q_\theta, 0) dq_\theta \\
&= \int_0^{2\pi} \int_0^\infty S(q', q_\theta, 0)\delta(q_r - q') q_r dq_r dq_\theta \\
&= \int_0^{2\pi} \int_0^\infty \underbrace{\mathcal{F}_{2D}[S(q', q_\theta, 0)]}_{I_1} \cdot \underbrace{\mathcal{F}_{2D}[\delta(q_r - q')]}_{I_2} r dr d\theta
\end{aligned} \tag{29}$$

using Parseval-Plancherel theorem (Eq. 24). We solve for I_1 using the central slice theorem (Eq. 26) through the xy-plane defined by $\mathbf{u}$ as

$$I_1 = \mathcal{F}_{2D}[S(q', q_\theta, 0)] = \mathcal{F}_{2D}[\mathcal{I}[\mathcal{F}_{3D}[P(r,\theta,z)]](\mathbf{u})] = \mathcal{L}[P(r,\theta,z)](\mathbf{u}) = \int_{-\infty}^{\infty} P(r,\theta,z) dz.$$

Noting that $\delta(q_r - q')$ is independent of θ, we can use the Hankel transform (Eq. 27) to evaluate I_2,

$$I_2 = \mathcal{H}[\delta(q_r - q')] = 2\pi \int_0^\infty \delta(q_r - q') J_0(2\pi q_r r) q_r dq_r = 2\pi q' J_0(2\pi q' r).$$

Therefore, inserting I_1 and I_2 into Eq. 29, we obtain

$$\mathcal{G}_{q'}[S(\mathbf{q})](\mathbf{u}) = 2\pi q' \int_{-\infty}^{\infty} \int_0^{2\pi} \int_0^\infty P(r,\theta,z) J_0(2\pi q' r) r dr d\theta dz. \tag{30}$$

Comparing Eq. 28 and Eq. 30, we note that the approximation depends on how close the zeroth-order Bessel function resembles the Dirac delta function. The width of J_0 is inversely proportional to q'. Hence, the larger b, the narrower the Bessel function, the closer the FRT approximation is to the exact ODF. This is clear from the shapes of the graph in Fig. 19. In [37], a QBI acquisition was achieved with $b = 4000 s/mm^2$.

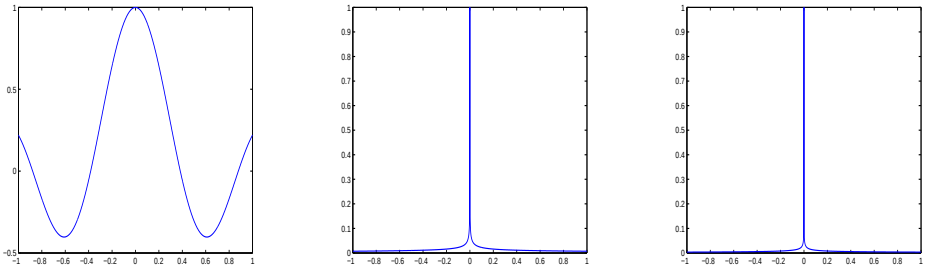

$z = 1$ $z = 1000$ $z = 4000$

Figure 19: Zeroth-order Bessel function $J_0(2\pi zX)$ approaches a Dirac delta function as z increases.

B Sequence of Gaussians is a delta sequence

Let $\delta_n(x) = \frac{n}{\sqrt{\pi}} e^{-n^2 x^2}$. We must show that

$$\lim_{n\to\infty} \int_{-\infty}^{\infty} \delta_n(x) f(x) dx = f(0)$$

for it to be a delta sequence.

Proof: Using the Taylor expansion of f(x) about $x = 0$, we have

$$\begin{aligned} \lim_{n\to\infty} \int_{-\infty}^{\infty} \delta_n(x) f(x) dx &= \lim_{n\to\infty} \int_{-\infty}^{\infty} \delta_n(x) \left(f(0) + f'(0)x + f''(0)\frac{x^2}{2!} + ... \right) dx \\ &= \lim_{n\to\infty} \left(f(0) \underbrace{\int_{-\infty}^{\infty} \delta_n(x) dx}_{I_1} + \sum_{k=1}^{\infty} \frac{f^{(k)}(0)}{k!} \underbrace{\int_{-\infty}^{\infty} x^k \delta_n(x) dx}_{I_k} \right) \end{aligned} \tag{31}$$

First, we show that $I_1 = 1$ for all n.

$$\begin{aligned} I_1 &= \frac{n}{\sqrt{\pi}} \int_{-\infty}^{\infty} e^{-n^2x^2} dx \\ &= \left(\frac{n}{\sqrt{\pi}} \int_{-\infty}^{\infty} e^{-n^2x^2} dx \frac{n}{\sqrt{\pi}} \int_{-\infty}^{\infty} e^{-n^2x^2} dx \right)^{1/2} \\ &= \left(\frac{n^2}{\pi} \int_{-\infty}^{\infty} e^{-n^2x^2} dx \int_{-\infty}^{\infty} e^{-n^2y^2} dy \right)^{1/2} \\ &= \left(\frac{n^2}{\pi} \int_{-\infty}^{\infty} \int_{-\infty}^{\infty} e^{-n^2(x^2+y^2)} dx dy \right)^{1/2} \\ &= \left(\frac{n^2}{\pi} \int_{0}^{2\pi} \left(\int_{0}^{\infty} e^{-n^2r^2} r dr \right) d\theta \right)^{1/2} \\ &= \left(\frac{n^2}{\pi} \int_{0}^{2\pi} \left(\frac{1}{2n^2} \right) d\theta \right)^{1/2} = 1 \end{aligned}$$

Now, we must show that the $\lim_{n\to\infty} I_k = 0$ for all $k \geq 1$. We use the known definite integral formula found in [33],

$$\int_0^{\infty} x^k e^{-ax^2} dx = \frac{\Gamma[(k+1)/2]}{2a^{(k+1)/2}},$$

where Γ is the Gamma function. In our case, we have an integral from $-\infty$ to ∞. If k is odd then the integrand is odd and I_k is zero. Hence, we have

$$\begin{aligned} I_k = \lim_{n\to-\infty} \frac{n}{\sqrt{pi}} \int_{-\infty}^{\infty} x^k e^{-n^2x^2} dx &= \lim_{n\to\infty} \frac{2n}{\sqrt{\pi}} \int_0^{\infty} x^k e^{-n^2x^2} dx \quad \text{for } k \text{ even} \\ &= \lim_{n\to\infty} \frac{\Gamma[(k+1)/2]}{n^k} = 0. \end{aligned}$$

Substituting back I_1 and I_k in Eq. 31 we obtain the desired result that

$$\lim_{n\to\infty} \int_{-\infty}^{\infty} \delta_n(x) f(x) dx = f(0),$$

showing that the sequence of Gaussians with decreasing variances, $\delta_n(x) = n/\sqrt{\pi}\exp(-n^2x^2)$, converges to the Dirac delta function $\delta(x)$.

C Exact ODF derivation From the Multi-Tensor Fiber Model

Assuming signal $S(\mathbf{u})$ is generated from the multi-tensor model for n fibers with relative weight p_k,

$$S(\mathbf{u}) = \sum_{k=1}^{n} p_k e^{-b\mathbf{u}^T D_k \mathbf{u}},$$

we want to derive the exact ODF for this fiber distribution. Recalling Eq. 1 which states that the signal is the Fourier transform $\mathcal{F}$ of the underlying probability density function $P(\mathbf{r})$, we first need to compute the inverse Fourier transform $\mathcal{F}^{-1}$ of $S(\mathbf{u})$ to obtain the corresponding PDF. We demonstrate the computation for a single Gaussian and then, by linearity, obtain the result for the general multi-Gaussian case. First, we will need the following inverse Fourier transform:

$$\mathcal{F}^{-1}[\exp\left(-bk^2\right)](x) = \frac{1}{2\pi}\sqrt{\frac{\pi}{b}}\exp\left(\frac{-x^2}{4b}\right). \tag{32}$$

Hence, the PDF obtained for a single Gaussian assuming diffusion tensor D with diagonal entry $[a, a, c]$ and signal formation given by $S(\mathbf{u}) = \exp(-b\mathbf{u}^T D\mathbf{u})$[1] is

$$\begin{aligned}
P(\mathbf{r}) &= \mathcal{F}^{-1}[\exp\left(-b\mathbf{u}^T D\mathbf{u}\right)] \\
&= \mathcal{F}^{-1}[\exp\left(-b(au_x^2 + au_y^2 + cu_z^2)\right)] \\
&= \mathcal{F}^{-1}[\exp\left(-bau_x^2\right)]\mathcal{F}^{-1}[\exp\left(-bau_y^2\right)]\mathcal{F}^{-1}[\exp\left(-bcu_z^2\right)] \\
&= \frac{1}{2\pi}\sqrt{\frac{\pi}{ba}}\exp\left(\frac{-x^2}{4ba}\right)\frac{1}{2\pi}\sqrt{\frac{\pi}{ba}}\exp\left(\frac{-y^2}{4ba}\right)\frac{1}{2\pi}\sqrt{\frac{\pi}{bc}}\exp\left(\frac{-z^2}{4bc}\right) \qquad \text{(Eq. 32)} \\
&= \frac{1}{8\pi^3}\sqrt{\frac{\pi^3}{b^3a^2c}}\exp\left(-\frac{1}{4b}\left(\frac{x^2}{a} + \frac{y^2}{a} + \frac{z^2}{c}\right)\right) \\
&= \frac{1}{\sqrt{(4\pi b)^3|D|}}\exp\left(\frac{-\mathbf{r}^T D^{-1}\mathbf{r}}{4b}\right)
\end{aligned}$$

Now, we can obtain the exact ODF by integrating the radial direction of the PDF (Eq 6). The ratio in front of the exponential in the final $P(\mathbf{r})$ expression is incorporated in a general normalization constant Z. We will also need the Gaussian integral formula $\int_0^\infty \exp(-r^2C)dr = 1/2\sqrt{\pi/C}$. Hence, for one fiber we have,

$$\begin{aligned}
\Psi_1(\mathbf{u}) &= \int_0^\infty P(r\mathbf{u})dr \\
&= \frac{1}{Z}\int_0^\infty \exp\left(\frac{-r^2\mathbf{u}^T D^{-1}\mathbf{u}}{4b}\right)dr \\
&= \frac{1}{Z}\sqrt{\frac{\pi b}{\mathbf{u}^T D^{-1}\mathbf{u}}} \qquad \text{(using the Gaussian integral formula)}
\end{aligned}$$

Thus, for n fibers, we have

$$\Psi(\mathbf{u}) = \sum_{k=1}^{n}\frac{p_k}{Z}\sqrt{\frac{\pi b}{\mathbf{u}^T D_k^{-1}\mathbf{u}}}$$

Now, we need to determine the Z for which the integral over the sphere of the ODF is 1. Rather than using the continuous closed form expression for $\int_{|\mathbf{u}|=1}(\mathbf{u}^T D^{-1}\mathbf{u})^{-1/2}d\mathbf{u}$, we prefer to estimate numerically this integral using the 81 sampling directions in order to obtain an accurate discrete normalization Z factor.

[1]Note that if we use the standard signal formation in q-space, $S(\mathbf{q}) = \exp(-\tau\mathbf{q}^T Dq)$ and $b = \tau|\mathbf{q}|^2$, we obtain the same expression with τ instead of b (as in [38, Eq.2]).

We can now compute the angular resolution limitation of the multi-tensor Gaussian fiber model. That is, we can find the relation between minimum angle between two synthetic fibers θ_{sep} and b-value assuming a HARDI experiment. We need to find for which separation angle θ_{sep} between two fibers do we start having a single ODF peak instead of two distinct peaks (assuming simple maxima detection by thresholding above 1/2). Note that the response function for a single fiber oriented in direction $\epsilon = (\theta, \phi)$ is simply $\Psi(\epsilon)$. Hence, for equal strength fibers and assuming that one fiber is along the z-axis, we want θ_{sep} for which

$$\frac{1}{2}\Psi(0,0) + \frac{1}{2}\Psi(\theta_{\text{sep}}, 0) \geq \frac{1}{2}$$

Note that in polar coordinates

$$\begin{aligned} \mathbf{u}^T D^{-1} \mathbf{u} &= \frac{1}{a}\left(\sin^2\theta\cos^2\phi + \sin^2\theta\sin^2\phi\right) + \frac{1}{c}\cos^2\theta \\ &= \frac{1}{a}\sin^2\theta + \frac{1}{c}\cos^2\theta \end{aligned}$$

Thus,

$$\frac{1}{2}\Psi(0,0) + \frac{1}{2}\Psi(\theta_{\text{sep}}, 0) \geq \frac{1}{2} \Longrightarrow \theta_{\text{sep}} \geq \sin^{-1}\left(\sqrt{\frac{(Z-\sqrt{c})^{-2} - 1/c}{(1/a - 1/c)}}\right)$$

For example, in our synthetic experiment, when $b = 1000$ s/mm^2, $\theta_{\text{sep}} = 29.7°$. If the angle between fibers is smaller, the exact ODF will only have a single peak instead of two. The relation

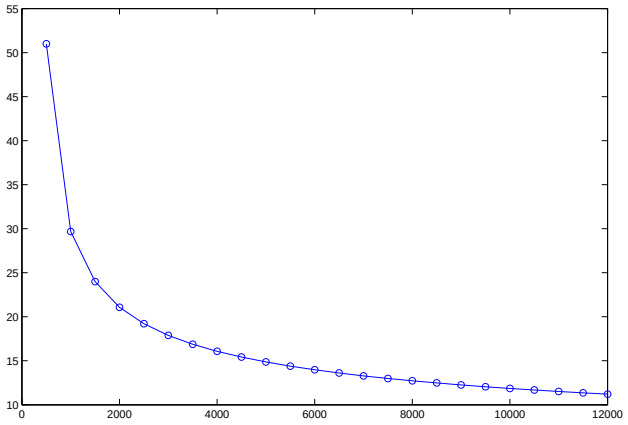

θ_{sep} in degrees vs b-value s/mm^2

Figure 20: Angular resolution limitation of the multi-tensor model assuming 81 HARDI sampling on the hemisphere and two equally weighted fibers with eigenvalues $[200, 200, 1700]$x10^{-6} mm^2/s.

between θ_{sep} and b-value is in Fig. 20. One can easily imagine that adding noise on the signal will produce even larger minimum angle.

D Defining the Fiber Response Profile for Sharpening

The main consideration is the creation of a viable response function $R(\theta)$ which will be used to transform the estimated ODF. Assuming that a Gaussian can describe the diffusion of water molecules for a single fiber, the corresponding expected response function is simply the ODF in the direction of the fiber which was derived the previous Appendix C. Thus, the response function of a fiber in direction ϵ is simply $\Psi(\epsilon)$. We are interested in finding a response profile and not necessarily an exact expression and hence use $\propto$ to indicate "proportional to". Referring to the previous Appendix, if θ represents the angle between point of evaluation $\mathbf{u}$ and direction of the fiber ϵ, we have

$$\begin{aligned} R(\theta) &\propto \sqrt{\pi b}\left(\frac{\sin^2\theta}{a}+\frac{1-\sin^2\theta}{c}\right)^{-\frac{1}{2}} \\ &\propto \left(\sin^2\theta\,(1-1/k)+1/k\right)^{-\frac{1}{2}} \end{aligned}$$

Therefore, we set the response function for an arbitrary Gaussian filter to be

$$R(t) = \left(t^2(1-1/k^2)+1/k^2\right)^{-\frac{1}{2}},$$

As seen in Fig. 21, the maximum occurs at k and we can therefore play with the "sharpness" of the profile. In a sense, k represents the anisotropy of the diffusion tensor D.

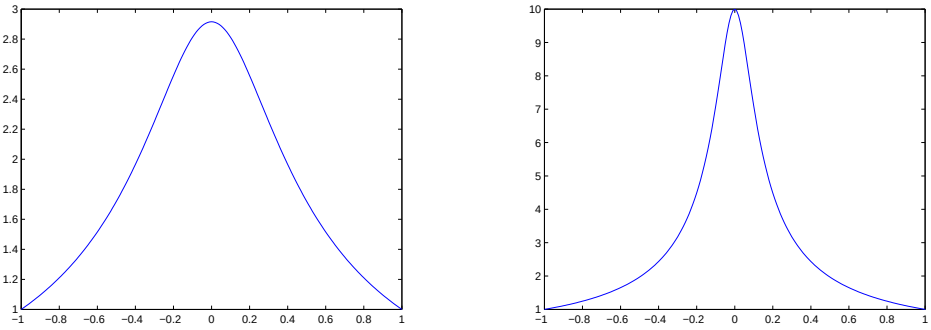

$R(t)$, $k = \sqrt{1700/200} = 2.9$ $\qquad$ $R_{\text{sharp}}(t)$, $k = 10$

Figure 21: Response function $R(t)$ and $R_{\text{sharp}}(t)$ of a Gaussian fiber.

Unité de recherche INRIA Sophia Antipolis
2004, route des Lucioles - BP 93 - 06902 Sophia Antipolis Cedex (France)

Unité de recherche INRIA Futurs : Parc Club Orsay Université - ZAC des Vignes
4, rue Jacques Monod - 91893 ORSAY Cedex (France)
Unité de recherche INRIA Lorraine : LORIA, Technopôle de Nancy-Brabois - Campus scientifi que
615, rue du Jardin Botanique - BP 101 - 54602 Villers-lès-Nancy Cedex (France)
Unité de recherche INRIA Rennes : IRISA, Campus universitaire de Beaulieu - 35042 Rennes Cedex (France)
Unité de recherche INRIA Rhône-Alpes : 655, avenue de l'Europe - 38334 Montbonnot Saint-Ismier (France)
Unité de recherche INRIA Rocquencourt : Domaine de Voluceau - Rocquencourt - BP 105 - 78153 Le Chesnay Cedex (France)

Éditeur
INRIA - Domaine de Voluceau - Rocquencourt, BP 105 - 78153 Le Chesnay Cedex (France)
http://www.inria.fr
ISSN 0249-6399